Probing *sd-fp* cross-shell interactions via terminating configurations in ^{42,43}Sc

C. J. Chiara,[1] M. Devlin,[1,*] E. Ideguchi,[1,†] D. R. LaFosse,[1] F. Lerma,[1,‡] W. Reviol,[1] S. K. Ryu,[1] D. G. Sarantites,[1] O. L. Pechenaya,[2] C. Baktash,[3] A. Galindo-Uribarri,[3] M. P. Carpenter,[4] R. V. F. Janssens,[4] T. Lauritsen,[4] C. J. Lister,[4] P. Reiter,[4,§] D. Seweryniak,[4] P. Fallon,[5] A. Görgen,[5,‖] A. O. Macchiavelli,[5] D. Rudolph,[6] G. Stoitcheva,[7] and W. E. Ormand[7]

[1]*Department of Chemistry, Washington University, St. Louis, Missouri 63130, USA*

[2]*Department of Physics, Washington University, St. Louis, Missouri 63130, USA*

[3]*Physics Division, Oak Ridge National Laboratory, Oak Ridge, Tennessee 37831-6371, USA*

[4]*Physics Division, Argonne National Laboratory, Argonne, Illinois 60439-4843, USA*

[5]*Nuclear Science Division, Lawrence Berkeley National Laboratory, Berkeley, California 94720, USA*

[6]*Department of Physics, Lund University, S-22100 Lund, Sweden*

[7]*Lawrence Livermore National Laboratory, P.O. Box 808, L-414, Livermore, California 94551, USA*

(Received 27 November 2006; published 4 May 2007; publisher error corrected 7 May 2007)

An experimental study of the lower *fp*-shell nuclei ^{42,43}Sc was performed via αpn and αp evaporation, respectively, from ^{20}Ne + ^{28}Si and ^{24}Mg + ^{24}Mg fusion-evaporation reactions. The experiments were conducted with the Gammasphere and Microball detector arrays. The level schemes of both nuclei have been extended considerably. Terminating states associated with the $f_{7/2}^n$ and $d_{3/2}^{-1}f_{7/2}^{n+1}$ configurations were identified in each nuclide and incorporated into detailed comparisons with neighboring nuclei and with shell model calculations. The energy differences between the terminating states provide a test of the *sd-fp* cross-shell interactions in these calculations.

DOI: 10.1103/PhysRevC.75.054305 PACS number(s): 23.20.Lv, 23.20.En, 21.60.Cs, 27.40.+z

I. INTRODUCTION

Nuclei in the lower *fp* shell, with $N \geqslant Z \geqslant 20$, are good candidates for studying the competition between single-particle and collective excitations. These nuclei have enough nucleons for collectivity to develop and compete with single-particle behavior, allowing the application of collective models, yet the nucleon numbers are sufficiently small to permit tractable shell model calculations as well. These various models, in general, provide a good description of spectroscopic properties throughout the entire *fp* shell. Comparisons of these models with the experimental data and with each other provide a means of testing the effective interactions used in shell model calculations and the strengths of the time-odd spin fields and the *ls* coupling used in a variety of Skyrme-force parametrizations [1]. In several cases, however, the available experimental data are insufficient to adequately define these parameters.

In the past two years, theoretical studies in this region have taken a new approach to better define these interactions and forces by examining the systematics of high-spin data [1–4]. Specifically, these studies consider terminating states associated with the $f_{7/2}^n$ and $d_{3/2}^{-1}f_{7/2}^{n+1}$ configurations (where n denotes the total number of $f_{7/2}$ valence particles present) which differ by the excitation of a $d_{3/2}$ nucleon across the N or $Z = 20$ shell gap into an $f_{7/2}$ orbital. This leads to a hole state in the $d_{3/2}$ subshell. Terminating states are those states that have the maximum angular momentum available from the complete alignment of the spins of the valence particles and holes for a given configuration, and are essentially pure single-particle states with strongly suppressed correlations beyond the mean field [5]. The difference in excitation energy for the terminating states of these two configurations, $\Delta E = E_x(d_{3/2}^{-1}f_{7/2}^{n+1}) - E_x(f_{7/2}^n)$, is predominantly determined by the size of the $N, Z = 20$ shell gap, which, in turn, is sensitive to the strength of the nucleon interactions [1,6]. Thus, measurements of this energy difference in a number of $A \approx 40$ nuclei provide a direct test of the strength of interactions used in modern calculations.

Prior to the current work, the terminating states of interest in ^{42}Sc and ^{43}Sc had not been conclusively identified. The former makes a particularly important contribution to the study because there is obviously a smaller data set available for $N = Z$ nuclei than for those with $N > Z$, and the two classes of nuclei have proven to exhibit different systematic trends [3,4]. In this paper, we present the experimental and theoretical details specifically pertaining to ^{42,43}Sc. It is worth noting that these results have already been incorporated into a recent continuation of the systematic theoretical study of the region [4]. Emphasis in this article is, thus, on the experimental analyses of these two nuclei (Secs. II–IV). In addition, comparisons between the observed level structures and shell model calculations are presented in Sec. V.

*Present address: LANSCE-3, MS H855, Los Alamos National Laboratory, Los Alamos, New Mexico 87545, USA.

†Present address: Center for Nuclear Study, University of Tokyo, 351-0198 Japan.

‡Present address: Department of Radiation Oncology, University of Maryland Baltimore, Baltimore, Maryland 21201, USA.

§Present address: Institut für Kernphysik, Universität zu Köln, Zülpicher Str 77, D-50937 Köln, Germany.

‖Present address: DAPNIA/SPhN, CEA-Saclay, F-91191 Gif-sur-Yvette Cedex, France.

II. EXPERIMENTAL DETAILS

Two experiments were performed to populate high-spin states in $N \approx Z \approx 20$ nuclei. One experiment produced ^{42}Sc and ^{43}Sc via the reactions ^{28}Si(^{20}Ne,αpn) and ^{28}Si(^{20}Ne,αp), respectively. An 84-MeV ^{20}Ne beam was provided by the Argonne Tandem-Linac Accelerator System (ATLAS) at Argonne National Laboratory. The target consisted of 0.5 mg/cm^2 of ^{28}Si supported by a $\sim$1 mg/cm^2 Ta foil facing the beam.

In the other experiment, the symmetric reaction ^{24}Mg + ^{24}Mg was used. A 94-MeV ^{24}Mg beam, provided by the 88-In. Cyclotron at Lawrence Berkeley National Laboratory, was directed onto a self-supporting ^{24}Mg target of nominal thickness 0.5 mg/cm^2. Both reactions created the same compound nuclei at similar excitation energies, but more angular momentum was brought into the compound system in the latter reaction.

In each experiment, emitted γ rays were detected with the Gammasphere array of Compton-suppressed HPGe detectors [7]; in the first (second) experiment, 101 (102) Ge detectors were in place, arranged in 16 rings of constant angle θ relative to the beam axis. Charged particles evaporated from the compound nuclei were detected with the Microball $\sim 4\pi$ array of 95 CsI(Tl) detectors [8], with efficiencies of $\varepsilon_p \approx 65\%$ for protons and $\varepsilon_\alpha \approx 50\%$ for α particles. The trigger conditions were set to a minimum "clean" (suppressed) γ-ray fold of three ($\gamma^{\geqslant 3}$). Pulse-height and timing signals from the Microball were not required in the trigger, but were accepted when present in coincidence with a $\gamma^{\geqslant 3}$ event. A total of 1.2×10^9 and 7.4×10^8 events were collected in the first and second experiment, respectively.

III. ANALYSIS

Events were selected offline in which exactly one proton and one α particle were detected (αp gate), yielding a subset of the data containing 2.0×10^8 and 9.9×10^7events for the two experiments. These events included $\varepsilon = \varepsilon_\alpha \varepsilon_p \approx 32.5\%$ of the αp charged-particle channel containing ^{42,43}Sc, as well as significant contamination from the $\alpha 2p$ and $2\alpha p$ channels. This contamination was reduced by subtracting out appropriately scaled amounts of the data sets gated on $\alpha 2p$ or $2\alpha p$, as described in Ref. [9].

Although the αpn + ^{42}Sc and αp + ^{43}Sc channels could not be further separated by particle gating in this experiment (no selectivity for neutrons), the following technique was used to enhance one channel over the other: The yrast lines in ^{42}Sc and ^{43}Sc are expected to be somewhat similar, so the amount of energy available for particle evaporation in both channels should also be similar. For ^{42}Sc, however, part of this energy goes to the undetected neutron. Thus, the sum of the detected charged-particle energies ΣE_{part} for ^{42}Sc will be less than that for ^{43}Sc. This is illustrated in Fig. 1, which shows distributions of ΣE_{part} versus the γ-ray sum energy H double gated on known γ rays in (a) ^{42}Sc and (b) ^{43}Sc. A clear separation of the two channels is seen around $\Sigma E_{\text{part}} \approx 25$ MeV. Coincidence gates were placed on the $\Sigma E_{\text{part}}(H)$ distributions in subsequent sorting of histograms to enhance either channel.

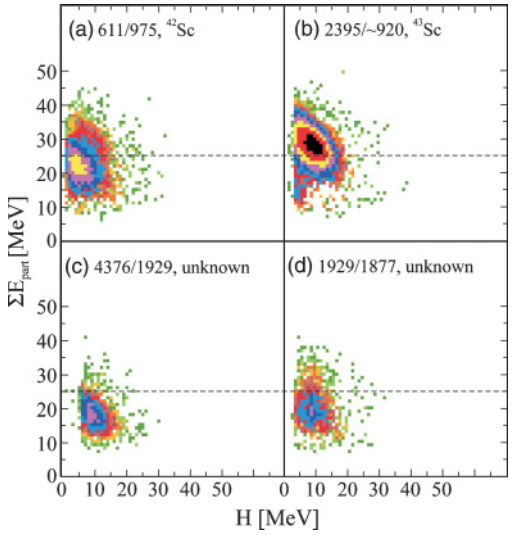

FIG. 1. (Color online) Sum of charged-particle energies ΣE_{part} vs γ-ray sum energy H for the ^{20}Ne + ^{28}Si reaction. The distributions are double gated by the transitions given in keV. (a) Distributions in ^{42}Sc. (b) Distributions in ^{43}Sc; ~920 includes the 912- and 928-keV transitions in ^{43}Sc. (c) and (d) are double gated on transitions of unknown origin (see Sec. IV A).

The data were unfolded into γ-γ coincidence events, and the γ-ray energies E_γ incremented into symmetrized E_γ-E_γ histograms (*matrices*). For both experiments, two $\Sigma E_{\text{part}}(H)$-gated matrices were created, one enhancing ^{42}Sc and the other enhancing ^{43}Sc. The γ-ray energies were corrected for the Doppler shift on an event-by-event basis; the measured charged-particle energies and Microball detector angles were used to include a correction for the momentum kicks provided to the residual nuclei by the emitted charged particles, which resulted in a sizable improvement in the measured γ-ray energy resolution [9]. To improve statistics, the data from the two experiments were combined into one matrix for each nucleus. The RADWARE analysis code ESCL8R [10] was used to project E_γ-gated, background-subtracted spectra from the coincidence matrices. These combined matrices were used in the construction of the ^{42,43}Sc level schemes discussed below.

The effectiveness of the $\Sigma E_{\text{part}}(H)$ gating is illustrated by the γ-ray spectra in Fig. 2. Both are gated on a region centered around 612 keV, encompassing the 611-keV peak in ^{42}Sc and the 613-keV peak in ^{43}Sc. The spectrum in the upper panel was created with a $\Sigma E_{\text{part}}(H)$ gating condition appropriate for ^{42}Sc; likewise for ^{43}Sc in the lower panel. The difference in relative intensities of the ^{42}Sc (asterisks) and ^{43}Sc (arrows) transitions is evident.

Several types of analysis were performed to determine the multipolarities of γ rays in both ^{42}Sc and ^{43}Sc. The first is an angular distribution (AD) analysis. Coincidence matrices were sorted from the αp-gated events such that the energies of γ rays detected at specific Gammasphere-ring angles, $E_\gamma(\theta)$, were incremented on one axis, while the energies of coincident γ rays detected at any angle, E_γ(any), were incremented on the other axis. Some adjacent rings of Gammasphere with similar angles were combined in the analysis to improve statistics; the 12 average angles used were $\theta = 34.5^\circ, 50.1^\circ,$

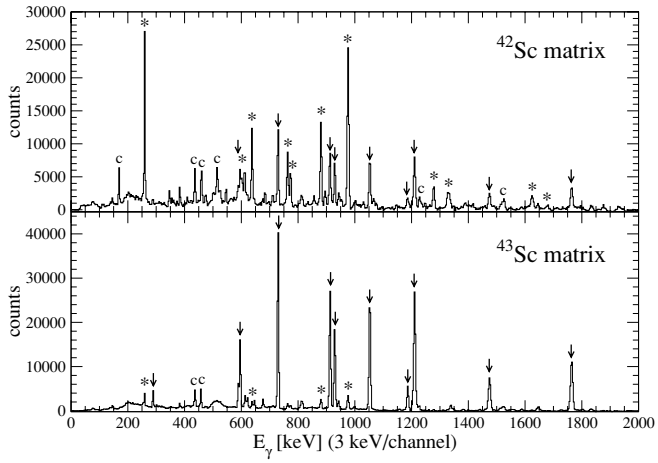

FIG. 2. Spectra gated around an energy of 612 keV and on $\Sigma E_{\rm part}(H)$ for ^{42}Sc and ^{43}Sc in the symmetrized E_γ-E_γ matrices (see text). Labeled peaks indicate transitions from ^{42}Sc (asterisks), ^{43}Sc (arrows), and known contaminants (c).

58.3°, 69.8°, 79.9°, 90.0°, 100.1°, 110.2°, 121.7°, 129.9°, 145.5°, and 162.7°. Data from the two experiments were sorted into separate matrices. Background-subtracted, angle-dependent spectra were created by gating on transitions on the E_γ(any) axis of the matrices. Peak areas for a given coincident transition were measured and normalized by the number of detectors at each angle, then fitted to the AD function $W(\theta) = a_0[1 + a_2 P_2(\cos\theta) + a_4 P_4(\cos\theta)]$. The ADs for several transitions were determined from both data sets. They were found to yield very similar a_2 and a_4 coefficients. Hence, the data from both experiments could be combined for greater statistics with consistent results for the fits. For the remaining AD analysis, the spectra projected from the matrices for both experiments, for a common E_γ(any) gate and angle θ, were statistically weighted by their relative efficiencies and combined. The peak fits were then performed on these combined spectra. Representative examples of the AD fits are given in the left column of Fig. 3.

For some γ rays with insufficient intensity for a meaningful AD analysis, directional correlation (DCO) or "DCO-like" analyses provided multipolarity information. DCO matrices with $E_\gamma(F/B)$ versus $E_\gamma(\sim 90^\circ)$ were created, where "F/B" includes the forward and backward angles $\theta \leqslant 50.1^\circ$ and $\theta \geqslant 129.9^\circ$, and "$\sim 90^\circ$" consists of the range $69.8^\circ \leqslant \theta \leqslant 110.2^\circ$. The DCO ratio is defined as $R_{\rm DCO} = I_\gamma(F/B, \sim 90^\circ)/I_\gamma(\sim 90^\circ, F/B)$, where $I_\gamma(i, j)$ is the intensity of a transition on the i axis measured in a spectrum produced by gating on a transition on the j axis. This ratio is dependent upon the multipolarity of the gating transition, however. DCO-like matrices with E_γ(any) versus $E_\gamma(F/B)$ and E_γ(any) versus $E_\gamma(\sim 90^\circ)$ were thus also created, in which spectra gated on transitions of any multipolarity could be summed. In this DCO-like analysis, r is the ratio $I_\gamma(F/B, any)/I_\gamma(\sim 90^\circ, \text{any})$ normalized by the number of detectors in each angle group. The expected values of these ratios, calculated as in Ref. [11], are given in Table I. Two sets of DCO and DCO-like matrices were created, gated on the $\Sigma E_{\rm part}(H)$ value for each nucleus.

Results of the AD and DCO analyses are included in Tables II and III. With a few exceptions (typically for high-energy γ rays), transitions were assumed to have $M1$, $E1$, or $E2$ multipolarities. These results were used to assign spins and parities for states identified in both nuclei.

IV. RESULTS

The most recent high-spin studies of ^{42}Sc prior to this work include lifetime measurements of γ rays from states up to $E_x \approx 4$ MeV in the ^{40}Ca(^{3}He,p) reaction by Roberson and Van Middelkoop [12], the ^{41}Ca(^{3}He,d) reaction by Vold *et al.* in which states below 6 MeV were observed [13],

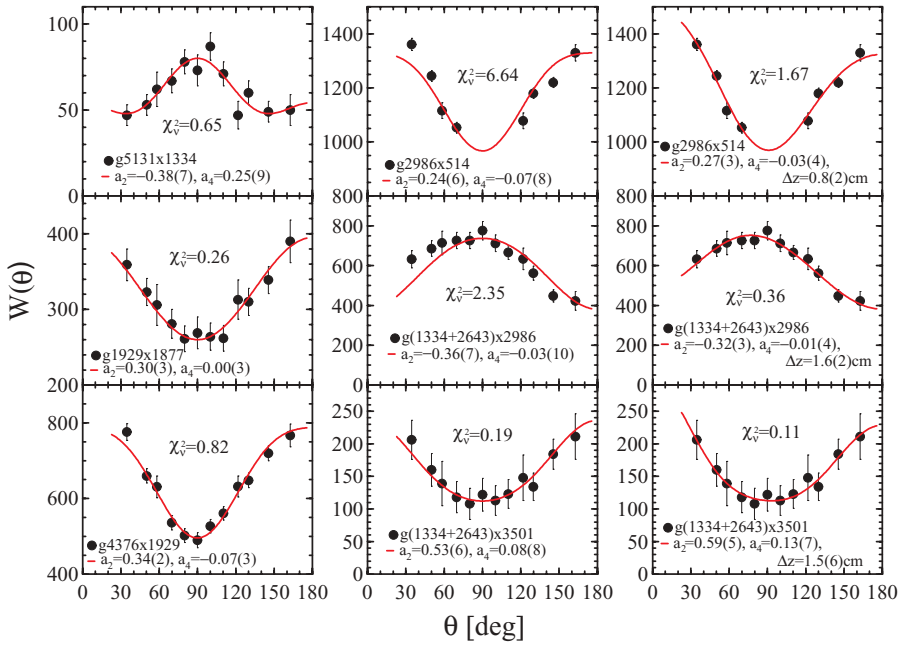

FIG. 3. (Color online) Measured angular distributions (ADs) and corresponding fits for several transitions in ^{42}Sc. Left column shows "normal" ADs, symmetric around 90°. Center column provides the skewed ADs, with symmetric fits, for the three transitions observed below the 4118-keV state (see Sec. IV A for details). Right column gives the same three ADs, but with skewed fits assuming a displacement along the beam direction by Δz from the target position. In the notation gGxX on each panel, G and X are the energies in keV of the gating and fitted γ rays, respectively. Also given are the a_2 and a_4 coefficients and reduced χ^2 from each fit. The 511-keV peak from e^+e^- annihilation interferes with the fits of the 514-keV γ ray at several angles near 90°; those angles were thus eliminated from the fit.

TABLE I. Approximate DCO (R_{DCO}) and DCO-like (r) ratios expected for the Gammasphere array, calculated assuming a Gaussian distribution for the population of spin substates with $\sigma_I/I = 0.3$. DCO ratios for a $\Delta I = 0$ pure dipole gate are not listed, but are very similar to those of the $\Delta I = 2$ quadrupole gate given in column 3. The DCO-like ratios in the last column have been normalized. DCO ratios for mixed $M1/E2$ transitions vary depending on the value of the mixing ratio; the values in the last two rows give the range of possible ratios for these mixed transitions.

Observed transition multipolarity	R_{DCO}, $\Delta I = 1$ pure dipole gate	R_{DCO}, $\Delta I = 2$ quadrupole gate	r (any gate)
$\Delta I = 2$ quadrupole	1.6	1.0	1.2
$\Delta I = 1$ pure dipole	1.0	0.6	0.8
$\Delta I = 0$ pure dipole	1.6	1.0	1.3
$\Delta I = 1$ mixed $M1/E2$	$0.5 < R_{DCO} < 1.9$	$0.3 < R_{DCO} < 1.2$	$0.4 < r < 1.5$
$\Delta I = 0$ mixed $M1/E2$	$1.1 < R_{DCO} < 1.7$	$0.6 < R_{DCO} < 1.1$	$0.8 < r < 1.3$

and the observation of γ rays from states up to 6.3 MeV in the ^{41}Ca(p,γ) proton capture study by Kikstra *et al.* [14]; these previous results have been compiled in Ref. [15]. High-spin states in the nucleus ^{43}Sc have been recently studied via γ-ray spectroscopy by Morikawa *et al.* [16], using the ^{27}Al(^{19}F,$p2n$) reaction, with excited states observed up to $E_x = 8.8$ MeV and to tentatively assigned spin and parity $I^\pi = (27/2^+)$. Earlier works by Poletti *et al.* [17] and Sheppard *et al.* [18] provided spin and parity assignments for several states in ^{43}Sc through angular distribution and polarization measurements of the deexcitation γ rays.

The current work improves considerably upon the previously known level schemes for both ^{42}Sc and ^{43}Sc. Figures 4 and 5 provide sample coincidence spectra gated on transitions assigned to ^{42}Sc and ^{43}Sc, respectively. The level schemes in Figs. 6 and 7 were constructed by considering such coincidence relations, as well as γ-ray energy sums and intensity balances, building upon the previously known level schemes. The dashed (red) lines on the figures indicate approximately those portions of the level schemes that had been previously identified. Details of these level schemes and distinctions from those that were previously published are addressed in the following two subsections. When energies of states or γ rays from previous works are discussed, the corresponding values fitted in the current work are quoted instead.

A. ^{42}Sc level scheme

The deduced properties of γ rays and states in ^{42}Sc are given in Tables II and IV, respectively. The states below the dashed line in the portion of Fig. 6 labeled (a) include those identified

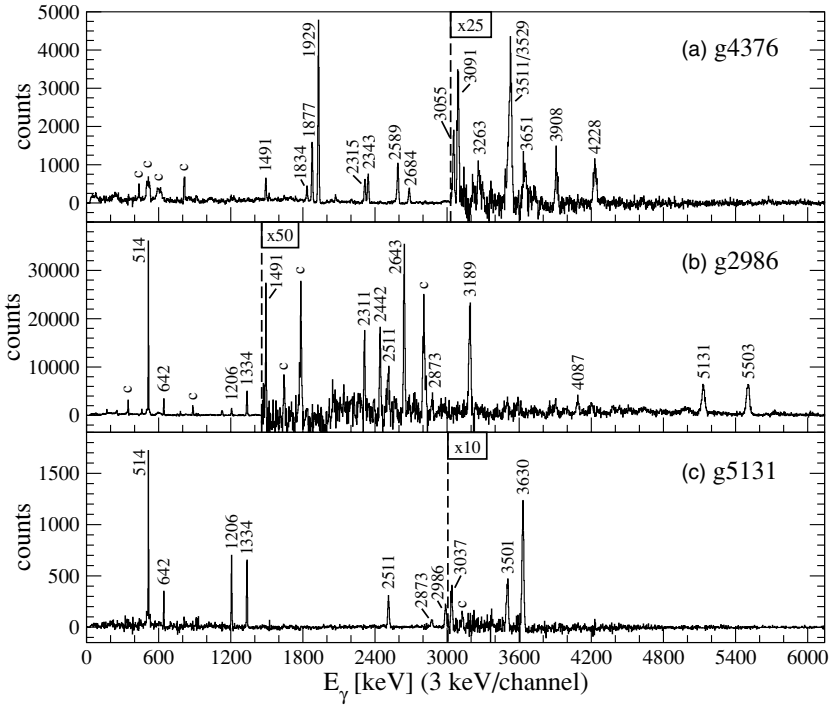

FIG. 4. Spectra for ^{42}Sc gated on γ rays at (a) 4376, (b) 2986, and (c) 5131 keV in the symmetrized ^{42}Sc E_γ-E_γ matrix (see text). Peaks are labeled with the energies in keV, or with a 'c' to indicate a contaminant. The counts to the right of the dashed line in each spectrum are scaled by the factors indicated on the panels.

TABLE II. Properties of γ rays identified in ^{42}Sc. First two columns give the energies in keV of the γ ray, E_γ, and of the state from which it decays, E_x. These energies were fitted in the combined data from both experiments. The quoted uncertainties on E_γ are statistical only; energies above ~3.5 MeV exceed the calibrated energy range and may have systematic errors of 1–2 keV. Columns three and four give the γ-ray intensities fitted in each experiment separately, as a percentage of the most intense transition (2986 keV). The last few columns provide the initial and final spins and parities of the states connected by each transition, the assigned multipolarities, and the results of the AD and DCO fits. Mixing ratios were not deduced, and transitions assigned $M1$ multipolarity may include some $E2$ admixture.

E_γ	E_x	$I_\gamma^{\mathrm{Ne+Si}}$	$I_\gamma^{\mathrm{Mg+Mg}}$	$I_i^\pi \rightarrow I_f^\pi$	$\sigma\lambda$	a_2	a_4	R_{DCO}
258.5(1)	1845	15.0(5)	18.0(6)	$3^{(+)} \rightarrow 2^+$	$M1$ or $E1$	−0.11(4)	0.01(5)	0.93(3)[a]
408.6(2)	3224	2.09(19)	2.29(24)	$(5^+) \rightarrow 4^+$	$(M1)$			
473.5(2)	3798	3.20(22)	3.5(3)	$(3^+) \rightarrow$				
514.0(1)[b]	4118	90(3)	89(3)	$10^- \rightarrow 8^-$	$E2$	0.24(6)[c]	−0.07(8)[c]	
601.1(1)	2188	4.30(22)	4.4(3)	$3^+ \rightarrow 2^+$	$M1$	−0.30(16)	−0.02(23)	0.90(12)[a]
611.1(1)	611	55(5)	66(5)	$1^+ \rightarrow 0^+$	$M1$	−0.12(2)	−0.02(3)	1.03(2)[a]
636.9(1)	2223	11.5(4)	14.3(5)	$3^+ \rightarrow 2^+$	$M1$	−0.12(3)	0.03(4)	0.96(4)[a]
642.2(1)	4247	10.3(4)	10.9(5)	$9^- \rightarrow 8^-$	$M1$	−0.49(16)	0.34(20)	0.99(20)[a]
682.9(2)	2269	2.72(19)	3.04(24)	$(1^+) \rightarrow 2^+$	$(M1)$			1.11(12)[a]
709.4(2)	2296	2.38(18)	2.82(22)	$\rightarrow 2^+$				
723.0(3)	3719	1.46(12)	1.74(17)	$(5)^+ \rightarrow (4)^+$	$(M1)$			
762.1(1)	2607	9.4(3)	11.3(4)	$4^{(+)} \rightarrow 3^{(+)}$	$M1$	−0.36(6)	0.10(9)	1.00(5)[a]
772.6(1)	2996	6.0(3)	7.9(4)	$(4)^+ \rightarrow 3^+$	$M1$			1.07(5)[a]
834.9(4)	3224	1.70(19)	1.95(24)	$(5^+) \rightarrow 3^+$	$(E2)$			
878.1(2)	2389	6.7(4)	8.0(5)	$3^+ \rightarrow 5^+$	$E2$[d]			
880.0(1)	1491	15.6(6)	18.1(8)	$3^+ \rightarrow 1^+$	$E2$[d]			
893.9(1)	1511	32(5)	32(5)	$5^+ \rightarrow 7^+$	$E2$			0.81(11)[e]
894.7(2)	3711	3.7(3)	3.8(3)	$(5^+) \rightarrow 4^+$	$M1$			0.70(12)[a]
922.7(3)	2434	3.5(3)	4.9(6)	$4^+ \rightarrow 5^+$	$M1$			1.27(13)[e]
942.9(2)	2434	3.47(21)	4.1(3)	$4^+ \rightarrow 3^+$	$M1$			1.03(15)[a]
975.4(1)	1587	33.8(11)	42.7(14)	$2^+ \rightarrow 1^+$	$M1$	−0.12(2)	0.00(3)	0.98(2)[a]
1000.8(3)	3224	1.46(12)	1.44(15)	$(5^+) \rightarrow 3^+$	$(E2)$			
1065.4(2)	2652	3.06(20)	4.1(3)	$(2) \rightarrow 2^+$	$(M1)$			
1145.7(4)	3798	1.20(13)	1.80(18)	$(3^+) \rightarrow (2)$	$(M1)$			
1206.0(1)	5452	34.8(11)	35.1(12)	$11^- \rightarrow 9^-$	$E2$	0.36(7)	0.02(9)	
1239.8(2)	4993	3.59(21)	4.4(3)	$9^+ \rightarrow 7^+$	$E2$			1.24(17)[e]
1270.1(1)	8095	10.5(4)	13.2(5)	$(10^-) \rightarrow (10^+)$	$(E1)$	0.40(10)	−0.15(13)	
1277.1(1)	3884	7.0(3)	8.7(3)	$6^{(+)} \rightarrow 4^{(+)}$	$E2$	0.29(11)	−0.16(16)	1.61(11)[a]
1305.6(3)	2816	2.58(22)	3.3(3)	$4^+ \rightarrow 5^+$	$M1$			0.64(10)[e]
1325.2(2)	2816	3.33(21)	3.9(3)	$4^+ \rightarrow 3^+$	$M1$			
1329.8(1)	3175	3.92(20)	5.1(3)	$(5^+) \rightarrow 3^{(+)}$	$(E2)$			1.57(11)[a]
1334.1(1)	5452	45.0(14)	48.1(15)	$11^- \rightarrow 10^-$	$M1$	−0.38(7)	0.25(9)	
1358.6(6)	3546	0.90(13)	1.00(18)	$(5^+) \rightarrow 3^+$	$(E2)$			
1491.0(1)	8799	9.9(4)	10.7(5)	$13^+ \rightarrow 11^+$	$E2$			
1587.1(7)	1587	2.7(3)	2.1(4)	$2^+ \rightarrow 0^+$	$E2$			
1597.8(1)	4884	7.4(4)	9.2(7)	$(8)^+ \rightarrow 7^+$	$(M1)$			
1623.2(1)	5507	4.91(20)	6.4(3)	$8^{(+)} \rightarrow 6^{(+)}$	$E2$	0.39(12)	−0.03(16)	1.53(13)[a]
1628.3(3)	4062	3.2(3)	3.5(4)	$(6^+) \rightarrow 4^+$	$(E2)$			
1676.8(4)	7184	1.57(13)	1.36(17)	$10^{(+)} \rightarrow 8^{(+)}$	$E2$			1.5(3)[a]
1713.3(2)	7677	2.92(18)	3.6(3)	$11^+ \rightarrow 9^+$	$E2$			
1736.4(6)	8921	1.92(25)	1.6(4)	$\rightarrow$				
1775.2(4)	3286	6.4(6)	5.7(8)	$7^+ \rightarrow 5^+$	$E2$			
1813.9(6)	3324	1.61(21)	2.1(3)	$\rightarrow 5^+$				
1830.3(5)	6825	1.88(17)	2.04(25)	$(10^+) \rightarrow 9^+$	$(M1)$			
1832.6(4)	3324	1.98(19)	1.98(24)	$\rightarrow 3^+$				
1834.3(2)	9511	6.1(3)	6.6(4)	$13^+ \rightarrow 11^+$	$E2$	0.32(6)	0.02(9)	
1856.1(12)	5402	0.33(12)	0.31(17)	$(7^+) \rightarrow (5^+)$	$(E2)$			
1876.6(1)	8799	20.9(7)	22.8(8)	$13^+ \rightarrow 11^+$	$E2$	0.30(3)	0.00(3)	
1929.3(1)	6922	63.5(20)	66.9(22)	$11^+ \rightarrow 9^+$	$E2$	0.34(2)	−0.07(3)	
1940.6(1)	6825	15.7(6)	18.0(8)	$(10^+) \rightarrow (8)^+$	$(E2)$	0.34(7)	−0.10(10)	
2055.7(7)	6118	1.66(22)	1.7(3)	$(8^+) \rightarrow (6^+)$	$(E2)$			

TABLE II. *(Continued.)*

E_γ	E_x	$I_\gamma^{\text{Ne+Si}}$	$I_\gamma^{\text{Mg+Mg}}$	$I_i^\pi \rightarrow I_f^\pi$	$\sigma\lambda$	a_2	a_4	R_{DCO}
2096.3(2)	8921	4.06(22)	4.4(3)	$\rightarrow (10^+)$				
2180.1(5)	9005	1.96(20)	2.7(3)	$\rightarrow (10^+)$				
2209.8(3)	5963	3.30(22)	4.4(3)	$9^+ \rightarrow 7^+$	$E2$	0.51(15)	fixed to 0	
2241.5(1)	3753	11.1(4)	12.9(6)	$7^+ \rightarrow 5^+$	$E2$	0.38(6)	−0.05(8)	
2300.2(5)	7185	3.9(4)	3.4(6)	$\rightarrow (8)^+$				
2310.8(2)	11932	6.3(3)	5.1(3)	$\rightarrow 12$				
2315.1(2)	7308	11.9(5)	12.3(6)	$11^+ \rightarrow 9^+$	$E2$	0.49(6)	−0.05(9)	
2342.5(1)	11854	14.2(5)	15.2(6)	$15^+ \rightarrow 13^+$	$E2$	0.20(4)	−0.12(6)	
2442.0(1)	10537	19.1(7)	20.2(8)	$(12^-) \rightarrow (10^-)$	$E2$	0.24(9)	−0.21(12)	
2511.0(2)	13094	7.9(3)	7.0(4)	$15 \rightarrow 13$	$E2$	0.40(12)	−0.04(17)	
2589.4(1)	9511	22.8(8)	23.4(8)	$13^+ \rightarrow 11^+$	$E2$	0.35(5)	−0.03(7)	
2642.7(1)	8095	22.2(7)	27.5(9)	$(10^-) \rightarrow 11^-$	$M1$	−0.36(7)	0.16(9)	
2668.4(2)	3286	14.7(18)	16(3)	$7^+ \rightarrow 7^+$	$M1$	0.09(5)	−0.15(7)	
2684.0(2)	7677	7.8(4)	7.7(5)	$11^+ \rightarrow 9^+$	$E2$	0.24(9)	−0.22(12)	
2872.6(3)	15967	2.34(14)	1.90(17)	$17 \rightarrow 15$	$E2$			1.03(31)[e]
2986.4(1)[b]	3604	100(4)	100(4)	$8^- \rightarrow 7^+$	$E1$	−0.36(7)[c]	−0.03(10)[c]	
3037.3(7)	13621	0.99(11)	0.72(15)	$\rightarrow 13$				
3054.9(5)	11854	2.59(19)	2.2(3)	$15^+ \rightarrow 13^+$	$E2$			
3091.4(3)	10013	4.17(21)	3.7(3)	$(13^+) \rightarrow 11^+$	$(E2)$	0.39(19)	0.15(25)	
3188.9(2)	7308	12.5(5)	11.6(6)	$11^+ \rightarrow 10^-$	$E1$			
3262.5(7)	10939	1.39(14)	1.18(23)	$\rightarrow 11^+$				
3480.4(6)	12401	1.97(16)	1.71(22)	$\rightarrow$				
3500.7(3)[b]	4118	19.9(9)	18.5(10)	$10^- \rightarrow 7^+$	$E3$	0.53(6)[c]	0.08(8)[c]	
3510.9(4)	13022	2.94(17)	3.32(24)	$\rightarrow 13^+$				
3529.1(3)	10451	5.6(3)	4.9(3)	$13^+ \rightarrow 11^+$	$E2$	0.49(15)	−0.06(23)	
3629.7(1)	4247	32.8(15)	31.9(18)	$9^- \rightarrow 7^+$	$M2$			1.04(14)[e]
3651.3(5)	12450	2.04(15)	1.84(19)	$\rightarrow 13^+$				
3907.5(5)	13419	2.32(14)	2.36(20)	$\rightarrow 13^+$				
4087.0(5)	8205	3.14(18)	2.67(24)	$\rightarrow 10^-$				
4227.5(6)	13026	2.33(18)	2.14(22)	$\rightarrow 13^+$				
4267.3(2)	4884	15.3(11)	20.0(18)	$(8)^+ \rightarrow 7^+$	$M1$	−0.08(7)	0.24(9)	
4375.8(1)	4993	75(6)	89(7)	$9^+ \rightarrow 7^+$	$E2$	0.35(5)	0.03(7)	
4640.4(6)	8887	2.66(20)	3.0(3)	$\rightarrow 9^-$				
5130.8(2)	10583	12.4(4)	11.2(4)	$13 \rightarrow 11^-$	$E2$ or $M2$	0.30(6)	−0.11(9)	
5346.5(7)	5963	4.0(5)	3.6(6)	$9^+ \rightarrow 7^+$	$E2$			
5502.6(2)	9621	9.4(3)	8.5(4)	$12 \rightarrow 10^-$	$E2$ or $M2$	0.27(10)	0.04(13)	1.80(31)[a]

[a]DCO ratio from spectrum gated on a stretched dipole transition.

[b]Energies and uncertainties for the 514-, 2986-, and 3501-keV γ rays as observed in the data. Actual energies should be slightly larger than these quoted centroids—they are shifted somewhat to lower values because of the lifetime of the 4118-keV state (see text).

[c]Values are under the assumption that decay occurs at the target position (see text). Fitting skewed ADs yields $a_2, a_4 =$ 0.27(3), −0.03(4) for 514 keV; −0.32(3), −0.01(4) for 2986 keV; and 0.59(5), 0.13(7) for 3501 keV.

[d]878- and 880-keV transitions could not be fitted because of contaminated spectra; multipolarities were taken from the literature.

[e]DCO ratio from spectrum gated on a stretched quadrupole transition.

levels common to both the literature [15] and the current work. Vold *et al.* [13] observed many additional non-yrast states through a (^{3}He,d) proton-pickup study, but without γ rays connecting them to lower-energy levels; the present work was not very sensitive to the observation of such states.

The portion of the ^{42}Sc level scheme labeled (b) in Fig. 6 deserves special mention. An 894-keV γ ray was identified in previous studies of ^{42}Sc decaying out of the 1511-keV 5^+ state in part (a) [15]. Figure 8(a) shows the 894-keV peak that is coincident with part (a) of the level scheme. A low-lying 894-keV γ ray was also observed in coincidence with transitions in part (b), as seen in Fig. 8(b). It is evident from the figure that the centroids of the 894-keV peaks coincident with both parts of the ^{42}Sc level scheme are consistent with them being a single, common γ ray, placed in the level scheme as given in Fig. 6. No other coincident transitions were found to be common to both parts (a) and (b) of the level scheme.

The presence of one candidate common transition is, in itself, insufficient evidence for assigning the new transitions

TABLE III. Same as Table II, but for ^{43}Sc. Intensities are normalized to the 912-keV transition. An 'r' superscript in the R_{DCO} column indicates results that come from the alternative DCO-like analysis.

E_γ	E_x	$I_\gamma^{\mathrm{Ne+Si}}$	$I_\gamma^{\mathrm{Mg+Mg}}$	$I_i^\pi \rightarrow I_f^\pi$	$\sigma\lambda$	a_2	a_4	R_{DCO}
135.5(1)[a]	3124	3.19(18)	1.73(8)	$19/2^- \rightarrow 15/2^-$	$E2$			
252.3(1)	7359	2.26(8)	2.04(9)	$25/2^+ \rightarrow 23/2^+$	$M1$			
287.9(1)	5519	1.96(7)	1.81(7)	$19/2^+ \rightarrow 17/2^+$	$M1$	−0.43(12)	0.09(17)	
288.4(1)	7107	0.58(3)	0.60(5)	$23/2^+ \rightarrow (21/2^+)$	$M1$			
456.7(1)	1338	3.60(14)	3.72(16)	$7/2^+ \rightarrow 5/2^+$	$M1$			
562.9(2)	1408	0.57(4)	0.45(6)	$7/2^- \rightarrow 5/2^-$	$M1$			
588.2(1)	3142	2.88(10)	3.02(11)	$13/2^+ \rightarrow 11/2^+$	$M1$			
595.1(1)	1933	10.8(3)	10.8(3)	$9/2^+ \rightarrow 7/2^+$	$M1$			
613.5(1)	3756	31.3(9)	32.4(10)	$15/2^+ \rightarrow 13/2^+$	$M1$	−0.42(8)	0.06(10)	
621.3(1)	2554	5.73(19)	5.94(21)	$11/2^+ \rightarrow 9/2^+$	$M1$	−0.43(8)	−0.01(10)	
645.4(1)	6819	1.33(7)	2.19(11)	$(21/2^+) \rightarrow 19/2^+$	$M1$			
653.9(2)	6173	0.66(6)	1.08(9)	$19/2^+ \rightarrow 19/2^+$	$M1$			
675.9(1)	7107	7.33(24)	7.3(3)	$23/2^+ \rightarrow 23/2^+$	$M1$	0.54(7)	0.21(10)	1.06(4)[b]
728.7(1)	881	50.8(19)	49.1(16)	$5/2^+ \rightarrow 3/2^+$	$M1$	−0.35(5)	0.13(6)	
764.3(1)	6284	2.29(12)	2.23(15)	$21/2^+ \rightarrow 19/2^+$	$M1$			0.70(23)[b]
766.9(2)	3756	0.97(5)	0.91(7)	$15/2^+ \rightarrow 15/2^-$	$E1$			0.73(12)[b]
771.6(4)	10856	0.53(6)	0.42(9)	$(27/2^-) \rightarrow 27/2^-$	$M1$			
804.4(3)	2636	0.90(8)	0.76(10)	$11/2^- \rightarrow 11/2^-$	$M1$			0.49(14)[b]
823.3(1)	7107	5.24(19)	4.86(20)	$23/2^+ \rightarrow 21/2^+$	$M1$			0.60(15)[b]
845.3(3)	845	0.29(4)	0.48(7)	$5/2^- \rightarrow 7/2^-$	$M1$			
860.4(2)	10856	0.51(4)	0.64(6)	$(27/2^-) \rightarrow 25/2^{(-)}$	$M1$			0.43(10)[b]
880.5(2)	881	1.65(10)	1.95(12)	$5/2^+ \rightarrow 7/2^-$	$E1$			
912.0(1)	6431	100(3)	100(3)	$23/2^+ \rightarrow 19/2^+$	$E2$	0.37(3)	0.03(4)	1.01(2)[b]
928.2(1)	7359	75.4(24)	76.2(24)	$25/2^+ \rightarrow 23/2^+$	$M1$	−0.18(3)	0.10(4)	0.68(1)[b]
933.0(5)	7107	0.93(7)	0.90(11)	$23/2^+ \rightarrow 19/2^+$	$E2$			
941.4(1)	6173	1.11(5)	1.82(8)	$19/2^+ \rightarrow 17/2^+$	$M1$			
951.0(3)	11807	1.23(6)	1.20(8)	$29/2^{(-)} \rightarrow (27/2^-)$	$M1$			0.70(11)[b]
971.5(1)	3960	2.18(8)	2.28(10)	$15/2^- \rightarrow 15/2^-$	$M1$			1.01(18)[b]
997.9(1)	18765	0.87(4)	0.65(4)	$(37/2) \rightarrow (35/2)$	$M1$			0.65(17)[b]
1043.6(1)	13117	1.19(6)	0.95(17)	$(31/2^-) \rightarrow (29/2^-)$	$M1$			0.64(15)[b]
1051.9(1)	1933	28.5(9)	29.4(9)	$9/2^+ \rightarrow 5/2^+$	$E2$	0.25(5)	−0.07(7)	
1052.9(4)	6284	0.07(4)	0.25(6)	$21/2^+ \rightarrow 17/2^+$	$E2$			
1075.6(3)	7359	0.70(7)	0.56(8)	$25/2^+ \rightarrow 21/2^+$	$E2$			
1157.5(1)	2988	15.2(6)	15.2(5)	$15/2^- \rightarrow 11/2^-$	$E2$	0.38(6)	−0.02(8)	1.05(5)[b]
1185.6(1)	1338	9.2(4)	9.1(4)	$7/2^+ \rightarrow 3/2^+$	$E2$	0.41(5)	−0.08(7)	
1202.1(1)	3756	5.76(19)	6.32(22)	$15/2^+ \rightarrow 11/2^+$	$E2$			
1209.7(1)	3142	30.9(9)	31.0(10)	$13/2^+ \rightarrow 9/2^+$	$E2$	0.27(3)	0.08(5)	
1216.1(1)	2554	4.45(17)	4.60(20)	$11/2^+ \rightarrow 7/2^+$	$E2$			
1227.1(3)	2636	2.37(19)	1.90(25)	$11/2^- \rightarrow 7/2^-$	$E2$			
1289.2(3)	14406	0.46(4)	0.44(7)	$(33/2^-) \rightarrow (31/2^-)$	$M1$			
1324.5(1)	3960	2.57(11)	2.52(13)	$15/2^- \rightarrow 11/2^-$	$E2$			0.96(10)[b]
1338.0(1)	1338	2.51(12)	2.41(13)	$7/2^+ \rightarrow 7/2^-$	$E1$			1.03(11)[b]
1360.6(4)	3293	0.65(6)	0.52(10)	$7/2^- \rightarrow 9/2^+$	$E1$			
1381.2(1)	10085	3.52(12)	3.37(14)	$27/2^- \rightarrow 25/2^{(+)}$	$E1$			0.47(3)[b]
1394.9(2)	4383	1.75(8)	1.43(11)	$17/2^{(-)} \rightarrow 15/2^-$	$M1$			0.54(5)[b]
1408.3(2)	1408	3.3(8)	2.1(5)	$7/2^- \rightarrow 7/2^-$	$M1$			1.19(23)[b]
1439.5(1)	9995	2.66(10)	2.02(11)	$25/2^{(-)} \rightarrow 23/2^-$	$M1$			0.66(4)[b]
1440.7(2)	19208	0.79(4)	0.75(4)	$(37/2^+) \rightarrow (35/2)$	$M1$			
1460.1(1)	12073	3.12(13)	2.26(14)	$(29/2^-) \rightarrow (27/2^-)$	$M1$			1.05(15)[c]
1472.5(1)	8832	35.9(11)	36.1(11)	$27/2^+ \rightarrow 25/2^+$	$M1$	−0.15(3)	0.10(4)	0.73(3)[b]
1476.0(1)	5232	5.49(20)	5.54(21)	$17/2^+ \rightarrow 15/2^+$	$M1$			
1529.0(1)	10085	4.63(16)	4.57(18)	$27/2^- \rightarrow 23/2^-$	$E2$			1.19(8)[b]
1586.9(3)	6819	0.39(4)	0.64(6)	$(21/2^+) \rightarrow 17/2^+$	$E2$			
1595.2(3)	8703	1.09(7)	0.95(9)	$25/2^{(+)} \rightarrow 23/2^+$	$M1$			
1650.3(1)	10085	10.7(4)	8.3(3)	$27/2^- \rightarrow 23/2^-$	$E2$	0.33(6)	0.06(8)	0.94(7)[b]
1724.8(2)	8832	2.10(10)	1.47(11)	$27/2^+ \rightarrow 23/2^+$	$E2$			

TABLE III. *(Continued.)*

E_γ	E_x	$I_\gamma^{\mathrm{Ne+Si}}$	$I_\gamma^{\mathrm{Mg+Mg}}$	$I_i^\pi \rightarrow I_f^\pi$	$\sigma\lambda$	a_2	a_4	R_{DCO}
1757.9(7)	12615	1.71(9)	1.62(11)	$(31/2)^- \rightarrow (27/2^-)$	$E2$			
1763.3(1)	5519	22.0(7)	23.0(7)	$19/2^+ \rightarrow 15/2^+$	$E2$	0.50(10)	−0.04(10)	
1791.2(1)	14406	6.06(21)	4.80(20)	$(33/2^-) \rightarrow (31/2)^-$	$M1$ or $E1$	−0.52(13)	−0.17(18)	0.47(7)[b]
1830.5(1)	1831	22.9(14)	37.7(24)	$11/2^- \rightarrow 7/2^-$	$E2$	0.36(3)	−0.01(4)	1.04(3)[b]
1833.6(2)	5794	2.85(13)	1.90(18)	$\rightarrow 15/2^-$				
1968.8(1)	12053	6.30(25)	4.89(24)	$29/2^{(-)} \rightarrow 27/2^-$	$(M1)$	−0.14(9)	0.06(12)	0.92(12)[b]
2058.7(2)	12053	1.23(7)	1.51(9)	$29/2^{(-)} \rightarrow 25/2^{(-)}$	$E2$			
2107.3(1)	6067	16.5(5)	15.1(5)	$19/2^- \rightarrow 15/2^-$	$E2$	0.37(4)	−0.08(6)	0.96(3)[b]
2129.7(1)	3960	15.1(5)	14.5(5)	$15/2^- \rightarrow 11/2^-$	$E2$	0.32(4)	−0.14(5)	1.03(4)[b]
2177.8(6)	10613	0.40(5)	0.32(6)	$(27/2^-) \rightarrow 23/2^-$	$E2$			1.13(39)[r]
2190.8(3)	12804	1.19(6)	0.60(6)	$\rightarrow (27/2^-)$				
2219.2(2)	9579	2.43(10)	1.28(11)	$(27/2^+) \rightarrow 25/2^+$	$M1$			
2228.0(2)	11807	1.76(8)	1.78(11)	$29/2^{(-)} \rightarrow (27/2^+)$	$E1$			
2271.8(1)	8703	9.9(3)	8.0(3)	$25/2^{(+)} \rightarrow 23/2^+$	$M1$ or $E1$	−0.31(16)	−0.22(21)	0.54(5)[b]
2353.2(3)	14406	1.57(8)	1.42(10)	$(33/2^-) \rightarrow 29/2^{(-)}$	$E2$			0.97(38)[r]
2368.6(5)	4301	0.99(7)	0.54(9)	$\rightarrow 9/2^+$				
2369.6(4)	8434	1.26(7)	1.26(9)	$23/2^- \rightarrow 19/2^-$				
2394.9(1)	5519	82(3)	79.4(25)	$19/2^+ \rightarrow 19/2^-$	$E1$	0.40(1)	0.01(2)	1.02(1)[b]
2418.3(2)	6173	1.18(6)	1.93(10)	$19/2^+ \rightarrow 15/2^+$	$E2$			
2488.2(1)	8556	13.9(4)	13.3(4)	$23/2^- \rightarrow 19/2^-$	$E2$	0.15(5)	−0.18(7)	1.14(7)[b]
2491.0(3)	8010	2.69(16)	2.17(18)	$\rightarrow 19/2^+$				
2503.1(1)	13117	3.68(14)	3.00(14)	$(31/2^-) \rightarrow (27/2^-)$	$E2$			1.73(20)[c]
2508.0(3)	14561	1.67(8)	0.71(9)	$31/2^- \rightarrow 29/2^{(-)}$	$M1$			
2530.4(1)	14451	3.02(12)	2.45(12)	$(29/2^+) \rightarrow 25/2^{(+)}$	$E2$			
2530.6(1)	12615	12.7(4)	10.6(4)	$(31/2)^- \rightarrow 27/2^-$	$(E2)$	0.18(6)	−0.33(8)	1.26(26)[b]
2598.0(1)	14406	2.91(11)	2.33(11)	$(33/2^-) \rightarrow 29/2^{(-)}$	$(E2)$	0.41(24)	0.35(32)	
2607.8(2)	13045	1.12(5)	1.11(6)	$(29/2^+) \rightarrow (25/2^+)$	$E2$			
2636.0(3)	2636	2.6(4)	2.3(4)	$11/2^- \rightarrow 7/2^-$	$E2$			
2644.5(5)	14451	0.97(6)	1.23(8)	$(29/2^+) \rightarrow 29/2^{(-)}$	$E1$			
2725.6(2)	10085	1.93(10)	2.36(11)	$27/2^- \rightarrow 25/2^+$	$E1$			0.68(14)[b]
2799.5(2)	11355	2.70(10)	2.53(12)	$27/2^- \rightarrow 23/2^-$	$E2$			0.99(10)[b]
2852.9(1)	17767	3.06(11)	2.57(11)	$(35/2) \rightarrow 31/2$	$(E2)$	0.10(18)	−0.38(28)	
2866.3(2)	15911	3.50(12)	2.89(13)	$(33/2^+) \rightarrow (29/2^+)$	$E2$			
2887.4(6)	9995	0.90(6)	1.10(9)	$25/2^{(-)} \rightarrow 23/2^+$	$E1$			
2920.2(10)	11355	0.39(5)	0.25(6)	$27/2^- \rightarrow 23/2^-$	$E2$			
2975.2(1)	11807	6.45(21)	5.66(20)	$29/2^{(-)} \rightarrow 27/2^+$	$M1$ or $E1$	−0.35(12)	0.10(16)	0.71(5)[r]
3038.1(5)	13123	1.27(9)	1.04(10)	$\rightarrow 27/2^-$				
3048.6(8)	6173	0.38(9)	0.63(15)	$19/2^+ \rightarrow 19/2^-$	$E1$			
3071.6(5)	10179	0.90(6)	0.57(8)	$\rightarrow 23/2^+$				
3079.0(1)	6067	4.92(17)	4.76(18)	$19/2^- \rightarrow 15/2^-$	$E2$	0.16(6)	−0.27(8)	1.07(5)[b]
3105.3(4)	11661	0.70(4)	0.58(5)	$\rightarrow 23/2^-$				
3124.2(3)	16708	1.03(5)	0.64(5)	$\rightarrow (29/2^+)$				
3147.7(2)	9579	2.80(11)	2.43(15)	$(27/2^+) \rightarrow 23/2^+$	$E2$			
3151.4(3)	9219	1.53(7)	1.62(9)	$(21/2^-) \rightarrow 19/2^-$	$(M1)$			1.14(15)[r]
3159.8(2)	6284	10.0(5)	8.2(8)	$21/2^+ \rightarrow 19/2^-$	$E1$			0.91(8)[c]
3205.3(3)	14561	2.09(9)	1.69(11)	$31/2^- \rightarrow 27/2^-$	$E2$			1.11(16)[r]
3253.9(1)	10613	8.5(3)	8.2(3)	$(27/2^-) \rightarrow 25/2^+$	$(E1)$	−0.15(4)	−0.08(6)	0.55(3)[b]
3296.0(4)	15911	1.24(7)	1.01(7)	$(33/2^+) \rightarrow (31/2)^-$	$E1$			
3298.8(3)	19208	1.58(7)	1.09(7)	$(37/2^+) \rightarrow (33/2^+)$	$E2$			
3307.6(2)	6431	8.9(3)	8.5(3)	$23/2^+ \rightarrow 19/2^-$	$M2$			
3329.9(2)	10437	2.04(9)	1.71(10)	$(25/2^+) \rightarrow 23/2^+$	$M1$			
3362.2(10)	7118	0.40(5)	0.26(7)	$\rightarrow 15/2^+$				
3469.8(2)	17921	1.74(8)	1.70(9)	$(31/2^+) \rightarrow (29/2^+)$	$(M1)$			0.77(10)[b]
3497.0(1)	10856	4.99(18)	4.54(18)	$(27/2^-) \rightarrow 25/2^+$	$(E1)$	−0.04(6)	−0.03(8)	0.59(6)[b]
3516.9(5)	7273	0.55(4)	0.48(5)	$\rightarrow 15/2^+$				
3586.9(5)	16704	0.47(3)	0.54(6)	$\rightarrow (31/2^-)$				
3635.4(3)	18196	1.31(6)	0.98(6)	$35/2^- \rightarrow 31/2^-$	$E2$			1.19(31)[r]

TABLE III. *(Continued.)*

E_γ	E_x	$I_\gamma^{\mathrm{Ne+Si}}$	$I_\gamma^{\mathrm{Mg+Mg}}$	$I_i^\pi \rightarrow I_f^\pi$	$\sigma\lambda$	a_2	a_4	R_{DCO}
3892.6(3)	11252	2.96(12)	2.67(13)	$\rightarrow 25/2^+$				
3906.6(5)	16711	0.58(5)	0.76(6)	$\rightarrow$				
3972.5(2)	12804	1.75(7)	1.37(7)	$\rightarrow 27/2^+$				
3997.1(3)	11355	1.23(7)	1.34(8)	$27/2^- \rightarrow 25/2^+$	$E1$			
4148.1(8)	12704	0.32(3)	0.16(3)	$\rightarrow 23/2^-$				
4213.0(3)	13045	1.88(7)	1.71(8)	$(29/2^+) \rightarrow 27/2^+$	$M1$			0.76(17)[r]
4341.7(3)	13045	1.66(7)	1.25(7)	$(29/2^+) \rightarrow 25/2^{(+)}$	$E2$			
4560.5(3)	11920	1.89(8)	1.76(8)	$25/2^{(+)} \rightarrow 25/2^+$	$M1$			1.02(8)[b]
4752.0(3)	13584	1.33(6)	1.23(7)	$(29/2^+) \rightarrow 27/2^+$	$(M1)$	−0.28(21)	0.19(31)	0.48(9)[r]
5310.5(1)	8434	13.8(10)	10.7(12)	$23/2^- \rightarrow 19/2^-$	$E2$	0.19(9)	−0.08(12)	1.42(22)[r]
5489.0(3)	11920	3.19(12)	2.43(11)	$25/2^{(+)} \rightarrow 23/2^+$	$M1$			0.84(11)[b]
5620.1(5)	14451	1.45(7)	1.82(8)	$(29/2^+) \rightarrow 27/2^+$	$M1$			
5684.9(4)	13045	1.52(7)	1.47(8)	$(29/2^+) \rightarrow 25/2^+$	$E2$			
6081.0(3)	14914	4.69(16)	4.05(14)	$31/2 \rightarrow 27/2^+$	$E2$ or $M2$	0.44(5)	−0.21(7)	1.19(12)[b]

[a]Depopulates 468-ns isomer.
[b]DCO ratio from spectrum gated on stretched quadrupole or $\Delta I = 0$ dipole transition.
[c]DCO ratio from spectrum gated on stretched dipole transition.

and states of part (b) to ^{42}Sc. Furthermore, one must also consider that, even if these were proven to be in ^{42}Sc, there may be a second 894-keV transition coincident with the transitions in part (b) that feeds the ground state rather than the 7^+ isomer ($E_x = 617$ keV, $t_{1/2} = 61.7$ s [15]). There are additional arguments, however, that confirm the placement of the transitions in the level scheme as given in Fig. 6: The charged-particle channel selection with the Microball indicates that these transitions are found in αp-gated spectra, but not in any appreciable amount in $\alpha 2p$- or $2\alpha p$-gated spectra. (A small amount can be expected due to misidentification of detector noise as an α particle or proton—see discussion in Sec. 3.6.5 in Ref. [9].) These observations limit the likely assignments to ^{42}Sc or ^{43}Sc. In the previous section, the

TABLE IV. Excitation energies, spins, and parities of states identified in ^{42}Sc. Tentative assignments are given in parentheses. Quoted uncertainties on energies are statistical only.

E_x	I^π	E_x	I^π	E_x	I^π
0.0(0)	0^+	3710.9(16)	(5^+)	8798.6(14)	13^+
611.1(2)	1^+	3719.0(17)	$(5)^+$	8887(3)	
617.0(13)	7^+	3752.7(14)	7^+	8921.1(19)	
1491.1(5)	3^+	3797.6(16)	(3^+)	9004.9(20)	
1511.0(12)	5^+	3884.2(7)	$6^{(+)}$	9511.3(14)	13^+
1586.5(3)	2^+	4062.2(22)	(6^+)	9621.0(19)	12
1845.0(4)	$3^{(+)}$	4118.4(14)	10^-	10013.4(22)	(13^+)
2187.7(7)	3^+	4246.6(14)	9^-	10451.1(21)	13^+
2223.4(4)	3^+	4884.2(14)	$(8)^+$	10537.0(15)	(12^-)
2269.5(11)	(1^+)	4992.8(13)	9^+	10583.3(17)	13
2295.9(12)		5402(3)	(7^+)	10939(4)	
2389.1(14)	3^+	5452.5(14)	11^-	11853.8(15)	15^+
2433.9(10)	4^+	5507.4(9)	$8^{(+)}$	11931.8(22)	
2607.1(5)	$4^{(+)}$	5963.2(17)	9^+	12401(4)	
2651.9(10)	(2)	6118(3)	(8^+)	12450(3)	
2816.3(10)	4^+	6824.8(14)	(10^+)	13022(3)[a]	
2996.0(6)	$(4)^+$	6922.0(13)	11^+	13026(3)[a]	
3174.8(9)	(5^+)	7184.3(23)	$10^{(+)}$	13094.2(19)	15
3224.4(11)	(5^+)	7185(3)		13419(3)	
3286.2(15)	7^+	7307.7(14)	11^+	13621(4)	
3324.1(15)		7676.8(15)	11^+	15967(3)	17
3546(2)	(5^+)	8095.0(14)	(10^-)		
3604.4(14)	8^-	8205(3)			

[a]Uncertainties are too large to rule out these being the same state.

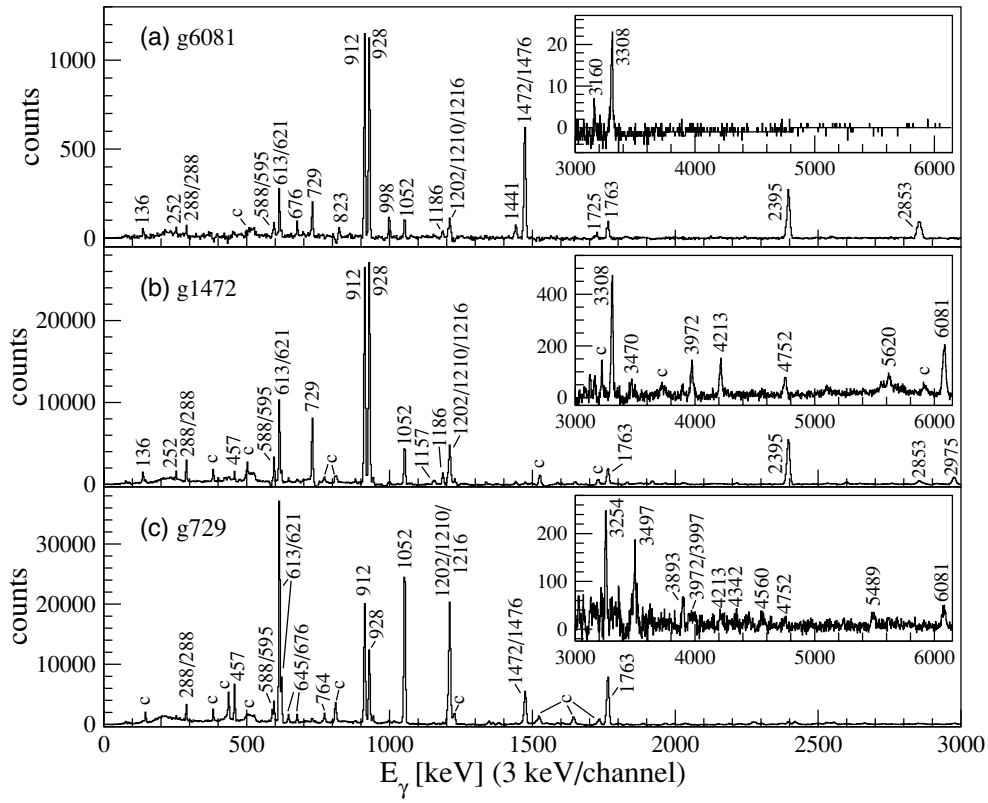

FIG. 5. Spectra for ^{43}Sc gated on γ rays at (a) 6081, (b) 1472, and (c) 729 keV in the symmetrized ^{43}Sc E_γ-E_γ matrix (see text). Peaks are labeled with the energies in keV, or with a 'c' to indicate a contaminant. Insets show the high-energy portion of each spectrum.

technique for enhancing ^{42}Sc or ^{43}Sc through $\Sigma E_{\rm part}(H)$ gating was discussed; the method can also be used in reverse, namely, by gating on unknown transitions and comparing the $\Sigma E_{\rm part}(H)$ distributions with those gated on known transitions in both nuclei. Such a comparison is made in Fig. 1. The distributions gated on the unknown transitions [panels (c) and (d)] fall below the line at ∼25 MeV, consistent with a ^{42}Sc assignment. Finally, the yrast lines in ^{42}Sc and ^{43}Sc, which are expected to be somewhat similar, can be compared to determine whether the transitions of part (b) feed the ground state or the isomer. The energies of states at each spin are plotted in Fig. 9 for both nuclei. Compared with ^{43}Sc [panel (a)], decay to the isomer in ^{42}Sc [+ symbols in panel (b)] is clearly far more likely than decay to the ground state [× symbols in panel (b)]. This is also consistent with the absence of an observed 894-keV state in previous studies of ^{42}Sc.

In part (a) of the ^{42}Sc level scheme, the AD and DCO measurements support many of the previous I^π assignments for the lower-lying states, and provide tentative assignments for states at higher energies. In addition, rigorous I^π assignments could be made for much of part (b) of the decay scheme. Results of the fits and assigned γ-ray multipolarities are given in Table II, and the corresponding I^π assignments are in Table IV. Assignments that are particularly important to the current study are those for the states with energies 3604 and 4118 keV in part (b) of the ^{42}Sc level scheme. As demonstrated in the center column of Fig. 3, the AD for the 2986-keV transition was found to be peaked at 90°, indicating stretched dipole character, whereas the 514- and 3501-keV γ rays are forward/backward peaked, suggesting assignments as a stretched quadrupole or as a $\Delta I = 0$ mixed $M1/E2$ transition in either case. The differences in spin for these possible scenarios are, however, inconsistent for the two parallel decay paths (514–2986 keV, or 3501 keV) between the 4118- and 617-keV states. For example, a $\Delta I = 0$ assignment for the 514-keV transition would imply a stretched-dipole assignment for the 3501-keV γ ray, but this is ruled out by the measured AD. It is worth noting that the fitted a_4 coefficient for the 3501-keV transition is consistent with a positive value, unlike $E2$ transitions which typically have values of $a_4 < 0$, and the a_2 coefficient is large and positive. This points to a different assignment as an $E3$ transition, which is also expected to have an AD that is forward/backward peaked with large positive a_2 and small positive a_4 coefficients [19]. The AD of an $E3$ transition should have a nonzero $a_6 P_6(\cos\theta)$ term as well, but this is generally rather small ($-0.05 < a_6 < 0$ for realistic cases with spin dealignment, $\sigma_I/I > 0.2$), and the current data are not sufficiently sensitive to this additional term. Including this term in the fits yields a negligible difference in the results for the a_2 and a_4 coefficients.

An $E3$ transition in competition with a 514-keV $E2$ transition raises the question of the lifetime of the 4118-keV state. Weisskopf estimates yield a lifetime of about 1 ns for the state, with a branching ratio $I_\gamma(514)/I_\gamma(3501) \sim 1$ consistent with the experimentally observed ratio of 4.5. With lifetimes on

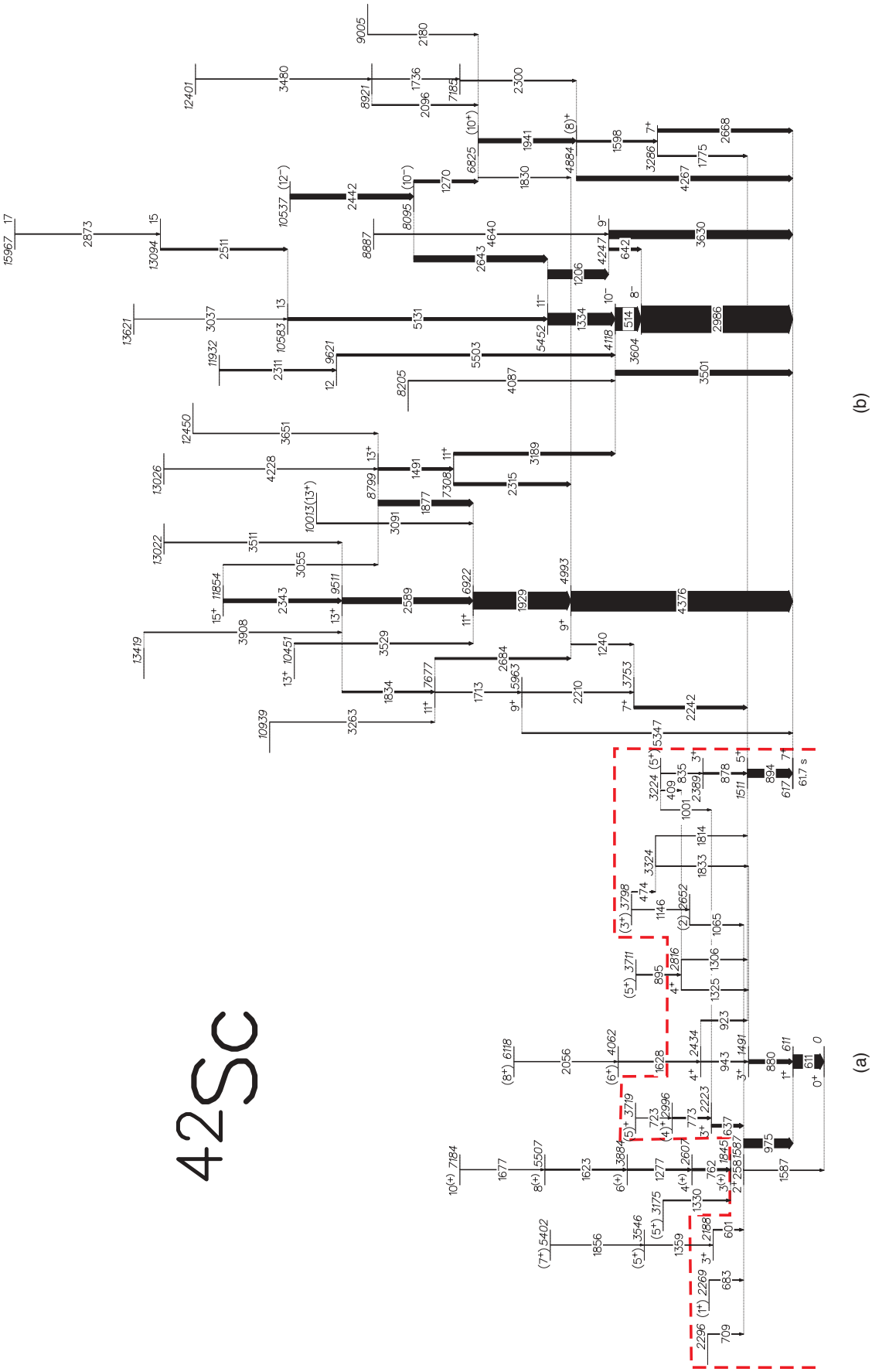

FIG. 6. (Color online) Level scheme for ^{42}Sc deduced from the combined data set in this work. Energies of states (in italics) and transitions are labeled in keV. Tentatively assigned spins and parities are given in parentheses. Dashed (red) line marks roughly the previously known portion of the level scheme.

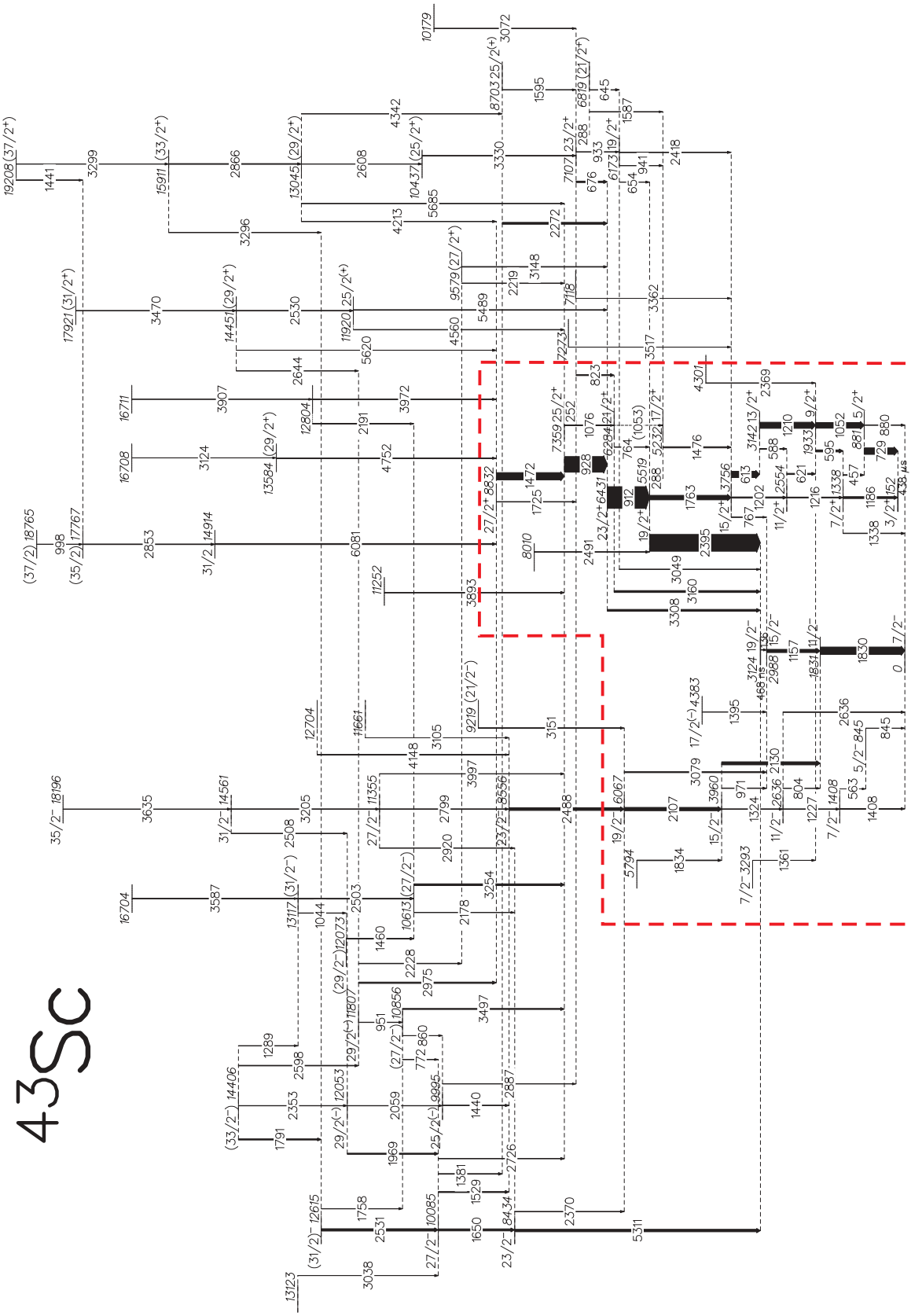

FIG. 7. (Color online) Same as Fig. 6, but for ^{43}Sc.

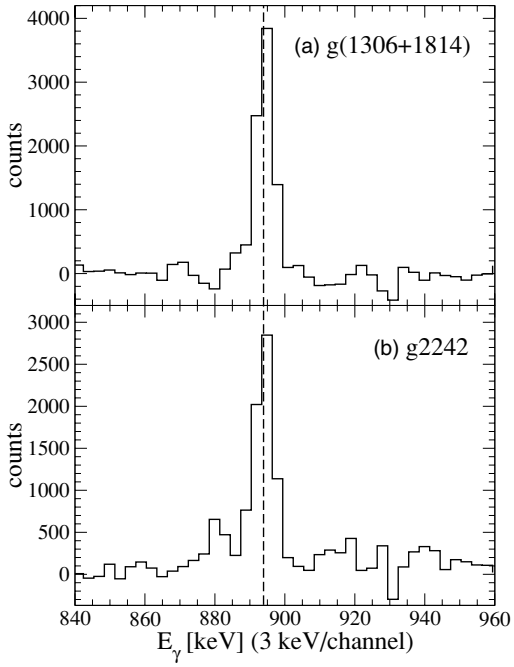

FIG. 8. Spectra gated on transitions in parts (a) and (b) of the ^{42}Sc level scheme. Gating energies are given in keV. Dashed vertical line marks the 894-keV transition that appears to be common to both parts of the level scheme.

the order of nanoseconds, in an experiment such as the present one that uses a thin target, one would expect the residues to travel centimeters away from the interaction point during the time before the state in question decays. In such circumstances, Gammasphere would no longer appear symmetric around 90°, due to a combination of the altered angle to each ring and the different effective efficiencies of the detectors. This would account for the slight skewing to forward angles of the ADs seen for the three transitions below the 4118-keV state, shown in the center column of Fig. 3. (Compare with the examples of "normal" ADs in the left column.) This effect is unlikely because of background or contamination issues, as all three transitions below the 4118-keV state exhibit it in several different sets of γ-ray-gated spectra. Incorporating this skewing effect into the AD fits, a rough estimate of the displacement from the target center can be established. A constant (average) displacement Δz was assumed in each case, rather than a time-dependent displacement following exponential decay. This is a sufficient approximation, as the two approaches yielded similar ADs and values of Δz in a test case. The skewed fits are provided in the right column of Fig. 3. There is not a large change in the fitted values of the a_i coefficients, but there is an improvement in the overall quality of the fits. Notably, the AD of the 3501-keV γ ray still is found to have large a_2, while the a_4 coefficient increased to a larger positive value, thus remaining consistent with an $E3$ assignment. The average displacement from center estimated in this way is about 1 cm, which is on the order of the Weisskopf lifetime estimate.

The applied correction for Doppler shifts assumes the residue is located at the center of Gammasphere. For residues that are displaced from the target, the wrong angles to the Ge detectors are used, resulting in centroid shifts that are not fully corrected. In other words, the peak centroids at each angle do not line up, with the largest differences in energy occurring between the detectors at forward/backward angles and those near 90°. The 2986- and 3501-keV transitions did not exhibit the 4- to 5-keV differences expected for a 1-cm displacement, but were found to have smaller shifts consistent with a lifetime of several tenths of a nanosecond. (A similar analysis for the 514-keV transition is prevented because of interference near 90°, where the effect is largest, from the 511-keV e^+e^- annihilation peak.) The statistical uncertainties for the centroids are large enough, however, that the deduced lifetime cannot be determined with better precision than that obtained through the AD measurement. The true lifetime is likely somewhere within the range determined by these two approaches, closer to 0.5 ns. Recall that this is not meant to be a rigorous determination of the lifetime, but rather more of an order-of-magnitude estimate.

The AD analysis allows for consistent spin and parity assignments for the 3604- and 4118-keV states as $I^\pi = 8^-$ and 10^-, respectively. The assignment for the 5452-keV state can be determined through the AD of the 1334-keV transition (top left panel of Fig. 3), which peaks at 90° like a stretched dipole. It is worth noting that the 1206- and 1334-keV γ rays decay from the 5452-keV state with very similar intensities.

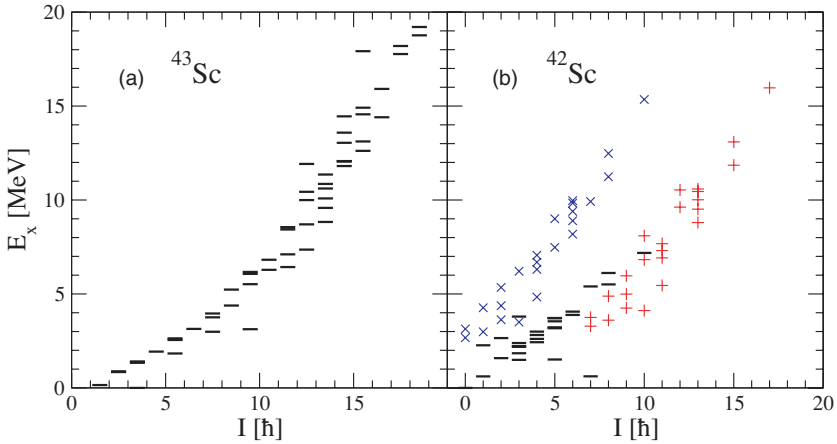

FIG. 9. (Color online) Excitation energy vs spin of states identified in (a) ^{43}Sc and (b) ^{42}Sc in this work. States with only tentatively assigned spins are also included. For ^{42}Sc, part (a) of the level scheme is indicated by bars; two scenarios shown for part (b) are decay to the ground state (×) or to the 7^+ isomer (+).

TABLE V. Same as Table IV, but for ^{43}Sc.

E_x	I^π	E_x	I^π	E_x	I^π
0.0(0)	$7/2^-$	6431.2(5)	$23/2^+$	12053.4(7)	$29/2^{(-)}$
152.0(5)	$3/2^+$	6818.6(7)	$(21/2^+)$	12073.3(8)	$(29/2^-)$
845.4(13)	$5/2^-$	7107.1(5)	$23/2^+$	12615.0(7)	$(31/2)^-$
880.8(5)	$5/2^+$	7118.0(15)		12704(3)	
1337.6(4)	$7/2^+$	7272.7(10)		12804.3(13)	
1408.3(11)	$7/2^-$	7359.4(5)	$25/2^+$	13044.5(10)	$(29/2^+)$
1830.6(3)	$11/2^-$	8010.2(8)		13116.7(9)	$(31/2^-)$
1932.6(5)	$9/2^+$	8434.5(6)	$23/2^-$	13123(3)	
2553.9(5)	$11/2^+$	8555.6(5)	$23/2^-$	13583.9(19)	$(29/2^+)$
2635.6(7)	$11/2^-$	8703.1(6)	$25/2^{(+)}$	14406.0(7)	$(33/2^-)$
2988.4(4)	$15/2^-$	8831.9(5)	$27/2^+$	14450.9(14)	$(29/2^+)$
3124.2(5)	$19/2^-$	9218.8(17)	$(21/2^-)$	14561.0(14)	$31/2^-$
3142.3(5)	$13/2^+$	9579.0(10)	$(27/2^+)$	14914.1(17)	31/2
3293.2(15)	$7/2^-$	9995.1(7)	$25/2^{(-)}$	15910.6(12)	$(33/2^+)$
3755.8(5)	$15/2^+$	10084.6(5)	$27/2^-$	16704(4)[a]	
3960.1(4)	$15/2^-$	10178.7(23)		16708(3)[a]	
4301.2(10)		10436.9(12)	$(25/2^+)$	16711(3)[a]	
4383.3(11)	$17/2^{(-)}$	10613.3(7)	$(27/2^-)$	17767.2(17)	(35/2)
5231.6(5)	$17/2^+$	10856.3(8)	$(27/2^-)$	17920.7(21)	$(31/2^+)$
5519.2(5)	$19/2^+$	11252.0(17)		18196.4(23)	$35/2^-$
5793.7(12)		11355.5(10)	$27/2^-$	18765.1(18)	(37/2)
6067.4(5)	$19/2^-$	11661(3)		19208.2(17)	$(37/2^+)$
6173.2(6)	$19/2^+$	11807.3(7)	$29/2^{(-)}$		
6283.8(6)	$21/2^+$	11920.3(12)	$25/2^{(+)}$		

[a]Uncertainties are too large to rule out two or more of these being the same state.

According to Weisskopf estimates, a pure $M1$ transition (1334 keV) is expected to be favored by orders of magnitude over an $E2$ transition with similar energy (1206 keV), in contrast to what is observed here. It is clear from the AD measurements, however, that the 1334-keV γ ray is not a pure transition—the a_4 coefficient is not consistent with zero, indicating a mixed $M1/E2$ character. A large $E2$ admixture for this transition could explain the observed branching ratio for the decay from the 5452-keV state. (The $M1$ strength for this transition is indeed found to be weak in shell model calculations.) This state has thus been assigned $I^\pi = 11^-$. These are the spin and parity quantum numbers expected for the terminating state of one of the configurations of interest in ^{42}Sc, as will be discussed in Sec. V. No other 11^- state was identified in this work.

B. ^{43}Sc level scheme

The deduced properties of γ rays and states in ^{43}Sc are given in Tables III and V, respectively. Most of the level sequences presented in Ref. [16] have been confirmed in this work. The 1259- and 3691-keV transitions and the (1648)–1510-keV cascade which were observed in Ref. [16] to feed the $19/2^-$, 468-ns isomer were not seen in the present study. The former measurement employed a backed target and an 800-ns coincidence window, allowing observation of coincidences across this isomer; unbacked targets were used in the current work, drastically reducing the likelihood of observing these coincidence relationships. Other transitions shown feeding this isomer in Ref. [16], namely, those with energies 2395, 3160, and 3308 keV, are observed in our data in coincidence with sequences of γ rays extending to high spins, but only very weakly in coincidence with the transitions below the isomer.

The only other feature of the ^{43}Sc level scheme proposed in Ref. [16] that was not confirmed in this work is the spin assignment of the 7107-keV state. Morikawa *et al.* assign this state as either $21/2^+$ or $25/2^+$ based on their so-called ADO angular distribution ratios for the 676- and 823-keV transitions [16]. We have instead assigned this state as $I^\pi = 23/2^+$. This assignment is based on the measured AD and DCO of the 676-keV transition and the DCO of the 823-keV transition (see Table III). Furthermore, a three-γ cascade (1725–933–2418 keV) was observed connecting the 8832-keV $27/2^+$ state to the 3756-keV $15/2^+$ state ($\Delta I = 6\hbar$). The most plausible scenario is that all three γ rays in that cascade are $E2$ transitions, thus giving the intermediate states, at 7107 and 6173 keV, $I^\pi = 23/2^+$ and $19/2^+$, respectively. This is not necessarily contradictory to the ADO measurements in Ref. [16]: there appear to have been only comparisons with pure quadrupole or dipole "calibration" ADO ratios, whereas some $E2$ admixture with $M1$ transitions would change the observed values. Additionally, the 823-keV transition was found to have a rather large uncertainty in that work.

Morikawa *et al.* observed most of the states forming the bandlike structure built on the $3/2^+$ isomer at 152 keV; although, for states above $15/2^+$, the spins and parities were only tentatively assigned [16]. (This structure may be viewed as a signature-partner structure.) The states at 7107 and 8703 keV observed in Ref. [16] are confirmed here, but they

are non-yrast levels that we have reassigned as a separate structure. A newly observed $21/2^+$ state at 6284 keV, fed by a 1076-keV γ ray from the $25/2^+$ state and decaying to the $19/2^+$ and $17/2^+$ states by 764- and (tentative) 1053-keV γ rays, respectively, completes the set of states in this band up to $27/2^+$. Our AD and DCO measurements now permit conclusive assignments of the spin and parity quantum numbers for all members of this sequence.

In addition to the bandlike structure mentioned above, a new collective structure was also observed in ^{43}Sc. It is a sequence of $E2$ transitions built upon the $7/2^-$ state at 1408 keV and extending up to the $35/2^-$ state at 18196 keV. Preliminary results from a lifetime analysis indicate that this band is associated with a moderately deformed shape; this structure will be discussed further in a separate publication [20].

V. DISCUSSION

As noted in the Introduction, the states of interest in this study are those based on the $f_{7/2}^n$ and $d_{3/2}^{-1}f_{7/2}^{n+1}$ configurations, specifically the terminating states of those configurations, and the theoretical discussion below will focus on these. For ^{42}Sc, the former configuration corresponds to a $\pi f_{7/2} \otimes \nu f_{7/2}$ coupling (which terminates at $I^\pi_{\max} = 7^+$). The latter configuration can be formed by either a proton or a neutron excitation, i.e., either the $\pi d_{3/2}^{-1} f_{7/2}^2 \otimes \nu f_{7/2}$ or $\pi f_{7/2} \otimes \nu d_{3/2}^{-1} f_{7/2}^2$ configuration ($I^\pi_{\max} = 11^-$) because of isospin symmetry. The 7^+ isomeric state at 617 keV [see Fig. 6(a)] had already been established as a member of the $\pi f_{7/2} \otimes \nu f_{7/2}$ multiplet in Ref. [21]. The 11^- state at 5452 keV [see Fig. 6(b)], as well as the 8^- to 10^- states below it (all yrast states), were observed for the first time in this work. They must involve a $d_{3/2}^{-1} f_{7/2}$ excitation across the N or $Z = 20$ shell gap in order to account for their negative parity.

For ^{43}Sc, the configurations under discussion are $\pi f_{7/2} \otimes \nu f_{7/2}^2$ (with $I^\pi_{\max} = 19/2^-$) and $\pi d_{3/2}^{-1} f_{7/2}^2 \otimes \nu f_{7/2}^2$ ($I^\pi_{\max} = 27/2^+$). The $19/2^-$ isomeric state at 3124 keV had been previously observed and associated with the $\pi f_{7/2} \otimes \nu f_{7/2}^2$ multiplet [22]. Finally, the spin and parity assignment for the 8832-keV state, tentatively proposed in Ref. [16] as $27/2^+$, has been confirmed conclusively in the present study. The levels forming the bandlike structure built on the 152-keV $3/2^+$ bandhead and extending up to this $27/2^+$ level are assigned as members of the $\pi d_{3/2}^{-1} f_{7/2}^2 \otimes \nu f_{7/2}^2$ configuration. It is worth noting that there are gaps of several MeV between the aforementioned levels and those with the next higher spins, supporting their interpretation as the terminating states of the configurations of interest.

Some features of the ^{43}Sc level scheme can be understood by considering the sequence of states in the neighboring isotones. Figure 10 compares the $\pi f_{7/2} \otimes \nu f_{7/2}^2$ and $\pi d_{3/2}^{-1} f_{7/2}^2 \otimes \nu f_{7/2}^2$ configurations in ^{43}Sc with the ground-state bands of ^{42}Ca ($\nu f_{7/2}^2$) and ^{44}Ti ($\pi f_{7/2}^2 \otimes \nu f_{7/2}^2$). For simplicity, only one signature-partner $E2$ sequence of the excited ^{43}Sc structure is displayed (see Sec. IV B). Note that an analogous comparison of ^{45}Sc with ^{44}Ca and ^{46}Ti was made in Ref. [25]. There is little overall change in the energies for the sequence of states when coupling an $f_{7/2}$ proton to the $\nu f_{7/2}^2$ band in ^{42}Ca to produce

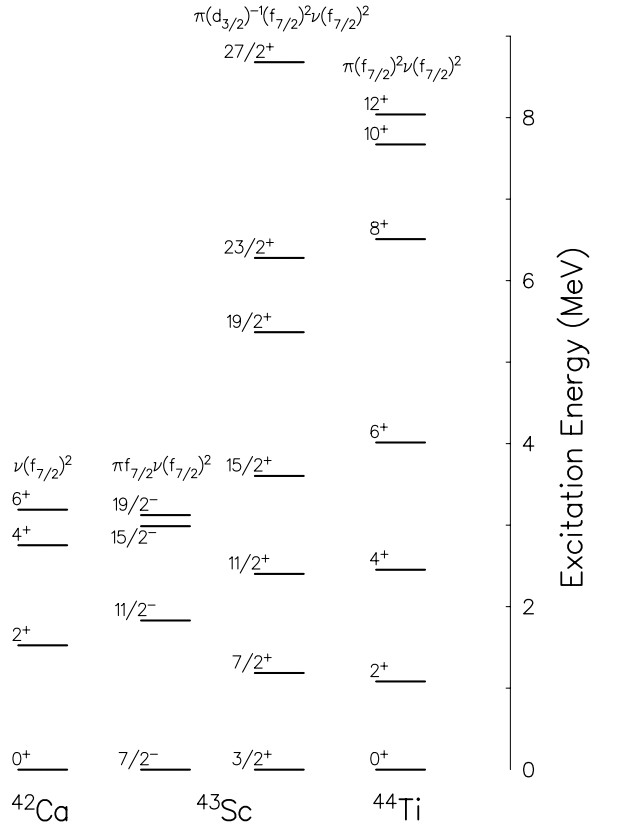

FIG. 10. Spectra of states for the ground-state bands of ^{42}Ca [23] and ^{44}Ti [24] in comparison with states identified as the $\pi f_{7/2} \otimes \nu f_{7/2}^2$ configuration and one signature of the $\pi d_{3/2}^{-1} f_{7/2}^2 \otimes \nu f_{7/2}^2$ configuration in ^{43}Sc, respectively. Energies are shown relative to the bandheads of each configuration.

the negative-parity states up to $19/2^-$ in ^{43}Sc. Likewise, the positive-parity levels up to $15/2^+$ in ^{43}Sc can be viewed as resulting from the coupling of a $d_{3/2}$ proton hole to the 0^+ to 6^+ states of the $\pi f_{7/2}^2 \otimes \nu f_{7/2}^2$ band in ^{44}Ti. At higher spins, the difference between the spectra of ^{43}Sc and ^{44}Ti is much more pronounced, as was also the case with ^{45}Sc and ^{46}Ti [25]. This difference will be further addressed below.

The ongoing systematic theoretical studies of terminating states in the $N \geqslant Z \geqslant 20, A \approx 40$ region includes a comparison between calculations using large-scale shell model (SM) and mean-field [Skyrme-Hartree-Fock (SHF)] approaches [1–4]. The earlier of these studies [1–3] did not include data for ^{42,43}Sc, as the states of interest were unavailable or only tentatively proposed at the time, but the current data were incorporated into a more recent continuation of the study [4]. Details of this systematic comparison of the two theoretical frameworks can be found in Ref. [4]; only a brief summary of the theoretical analyses, and those results relating specifically to ^{42,43}Sc, are included here.

For the intruder configurations, which originate from particle-hole excitations with respect to a ^{40}Ca core, the *fp* shell-model space is not sufficient to describe the spectrum of states. Therefore, the SM calculations were performed in the *sd-fp* configuration space, but limited to one-particle one-hole (1p1h) cross-shell excitations due to the large model

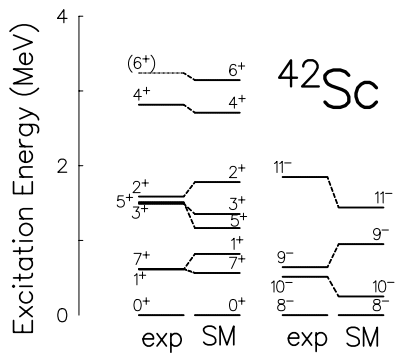

FIG. 11. SM calculations of the $f_{7/2}^{n}$ (left) and $d_{3/2}^{-1}f_{7/2}^{n+1}$ (right) configurations in ^{42}Sc compared with the corresponding observed structures (see text). Dashed (6^+) state at 3240 keV was not observed in the current data, but was taken from the literature [13].

space dimensions involved. These calculations were carried out using the code ANTOINE [26]. The matrix elements are those used in Ref. [27], but with the *fp*-shell two-body matrix elements replaced with those of the FPD6 interaction [28]. These calculations are similar to the ones for ^{43}Ca and ^{45}Sc in Ref. [25], apart from a ∼4% reduction in the *sd* interaction channel.

Figures 11 and 12 compare states calculated with the SM with the experimentally observed levels for the ground-state

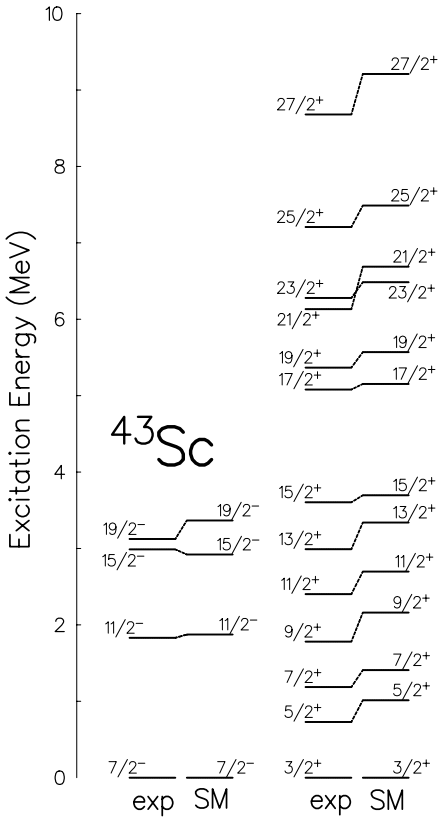

FIG. 12. SM calculations of the $f_{7/2}^{n}$ (left) and $d_{3/2}^{-1}f_{7/2}^{n+1}$ (right) configurations in ^{43}Sc compared with the corresponding observed structures (see text).

$(f_{7/2}^{n})$ and excited $(d_{3/2}^{-1}f_{7/2}^{n+1})$ configurations in ^{42}Sc and ^{43}Sc, respectively. The states shown are those with the dominant configuration of interest, and need not necessarily be yrast. Note that the even-spin states of the $\pi f_{7/2}\otimes\nu f_{7/2}$ configuration in ^{42}Sc are the analog states of the $\nu f_{7/2}^{2}$ sequence in ^{42}Ca [23] (see left side of Fig. 10) and the $\pi f_{7/2}^{2}$ sequence in ^{42}Ti [29]. (A comparison of these analog states can be found in, e.g., Fig. 4 of Ref. [13].) The excitation energies of the intruder states in Figs. 11 and 12 are given relative to the lowest states of those configurations, not the ground states. The overall features of the two sets of level sequences are well reproduced, with, in most cases, excitation energies in agreement to within a few hundred keV and the correct grouping of states.

In ^{42}Sc, the sequence of states in the calculated ground-state configuration differs slightly from the observed order. These differences involve the interchange of the 1^+ and (terminating) 7^+ states and the 3^+ and 5^+ states. These pairs of states, however, are nearly degenerate in the data (6 and 20 keV separation, respectively). The negative-parity states up to $I_{\rm max}^{\pi} = 11^-$ are related to the 1p1h excitation from the *sd* to the *fp* shell. Here, the order of states is reproduced, though the 8^- and 10^- states are calculated to be close in energy, whereas experimentally the 9^- and 10^- states are grouped together. As discussed in Ref. [4], the calculated structure of $N = Z$ nuclei can be affected by the interaction used in the SM studies. Correlations from the $T = 0$ *np*-pairing channel are expected to play a role in $N = Z$ nuclei. Improvements to the calculated spectra are anticipated once these correlations are included by the addition of multiparticle-multihole excitations.

In the SM description, the negative-parity structure of ^{43}Sc has one proton and two neutrons in the $f_{7/2}$ shell, and the maximum aligned state has $I_{\rm max}^{\pi} = 19/2^-$. The positive-parity states up to $I_{\rm max}^{\pi} = 27/2^+$ can be associated with a hole in the *sd* shell. As shown in Fig. 12, the SM energies for the ground-state and excited configurations are in very good agreement with the experimental data, although the calculated energies for the latter are systematically higher than the experiment. The gaps in the level scheme between $15/2^+$ and $17/2^+$ and between $25/2^+$ and $27/2^+$ are also well reproduced. The intermediate-spin states, between $15/2^+$ and $27/2^+$, are those shown in Fig. 10 to differ most from the corresponding ^{44}Ti ground-state band.

These differences between ^{43}Sc and ^{44}Ti, and the observed gaps in the ^{43}Sc excited structure, could possibly be explained by the following consideration: Although the $27/2^+$ terminating state of the excited structure is attributed solely to the proton-excited $\pi d_{3/2}^{-1}f_{7/2}^{2}\otimes\nu f_{7/2}^{2}$ configuration, the lower-spin states may also include a sizable contribution from the neutron-excited $\pi f_{7/2}\otimes\nu d_{3/2}^{-1}f_{7/2}^{3}$ configuration (which terminates at $I_{\rm max}^{\pi} = 25/2^+$). The former configuration can be created by coupling a $d_{3/2}$ proton hole to the $\pi f_{7/2}^{2}\otimes\nu f_{7/2}^{2}$ ground-state configuration in ^{44}Ti, producing the very similar level scheme at low spins. The latter configuration, however, cannot be formed by the simple coupling of a single particle or hole to this ^{44}Ti band. A significant increase in the neutron-excitation component of the wave function for the intermediate-spin states might manifest itself through the observed differences in the level schemes. The gaps in the ^{43}Sc

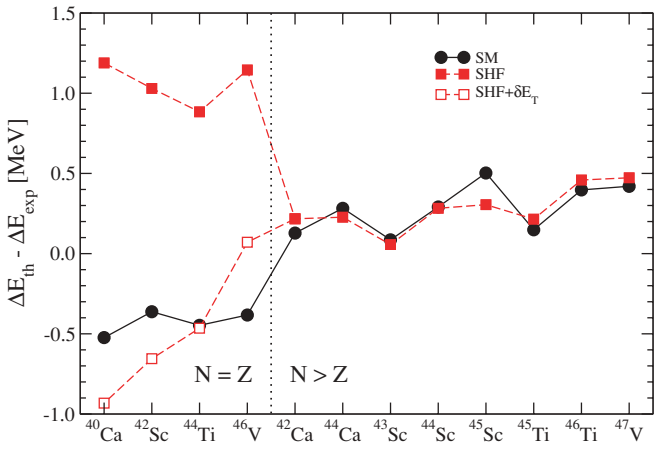

FIG. 13. (Color online) Theoretical energy differences (ΔE_{th}) relative to experimental energy differences (ΔE_{exp}), adapted from Fig. 2 of Ref. [4]. δE_T is an isospin correction term in the SHF calculations for the $N = Z$ nuclei, as described in Ref. [4]. SHF results are shifted up by 480 keV for comparison with the SM calculations.

structure may also be related. Preliminary results suggest that an increased contribution from neutron excitations is supported by the SM calculations, but this behavior requires further exploration.

The differences in excitation energies of the terminating states of the $f_{7/2}^n$ and $d_{3/2}^{-1} f_{7/2}^{n+1}$ configurations from the calculations (ΔE_{th}) and from experiment (ΔE_{exp}) were compared, for ^{42,43}Sc and all other neighboring nuclei for which the data were available, in Ref. [4]. The results of that comparison are summarized here, and an adapted version of Fig. 2 of Ref. [4] is given in Fig. 13 to aid in this discussion. As noted in Ref. [4], the SM calculations (filled circles) overestimate the data by an average of 280 keV in the $N > Z$ nuclei (to the right of the dotted line in Fig. 13), but underestimate the data by about 410 keV in $N = Z$ cases (left of the dotted line). SHF calculations were also carried out for these nuclei, using a slightly modified version [1] of the SkO parametrization of the Skyrme force (filled squares in Fig. 13). Once a correction was introduced to restore isospin symmetry (see Ref. [4] for details), the values of ΔE_{th}-ΔE_{exp} for the SHF calculations closely followed the same trends as the SM calculations, with an overall energy offset that could be justified by a change in the size of the $N = Z = 20$ shell gap (SM) or in the spin-orbit term (SHF)—see the open squares in Fig. 13. These new data for ^{42}Sc and ^{43}Sc fit well with the systematics. Data for the former are particularly useful in the theoretical analysis, because ^{42}Sc is one of the few available $N = Z$ cases, which provide a test of the accuracy of existing $T = 0$ pair correlations in the calculations [4,30]. Improvements to the SM calculations in this systematic study are in progress and will be presented in a forthcoming theoretical paper [31].

VI. CONCLUSIONS

The level schemes of ^{42,43}Sc have been extended to considerably higher excitation energies and spins. Rigorous spin and parity assignments were proposed for many levels on the basis of angular-distribution and DCO measurements. These assignments enabled us to identify the terminating states of the $f_{7/2}^n$ and $d_{3/2}^{-1} f_{7/2}^{n+1}$ configurations. The energy differences between these terminating states are part of a systematic comparison of experimental data with SM and SHF calculations in lower *fp*-shell $N \geqslant Z \geqslant 20$ nuclei. The SM calculations, included here for these two nuclei, reproduce the observed sequences of states reasonably well. The terminating-state energy differences are consistent with the systematics, as shown in Ref. [4]. The new results for ^{42}Sc further emphasize the need to examine closely the $T = 0$ correlations in the calculations for $N = Z$ nuclei.

ACKNOWLEDGMENTS

Helpful discussions with W. Satuła are gratefully acknowledged. This work was supported in part by the U.S. Department of Energy (DoE), Office of Nuclear Physics, under Grant No. DE-FG02-88ER-40406 (Washington U.), Contract No. DE-AC02-06CH11357 (Argonne National Laboratory), Contract No. DE-AC05-00R22725 with UT-Battelle (Oak Ridge National Laboratory), Contract No. DE-AC03-76SF00098 (Lawrence Berkeley National Laboratory), and Contract No. W-7405-ENG-48 under the auspices of the DoE by the University of California (Lawrence Livermore National Laboratory). Additional support was provided by the Swedish Research Council (Lund U.).

[1] Honorata Zduńczuk, Wojciech Satuła, and Ramon A. Wyss, Phys. Rev. C **71**, 024305 (2005).
[2] W. Satuła, R. Wyss, and H. Zduńczuk, Eur. Phys. J. A **25**, S01 551 (2005).
[3] G. Stoitcheva, W. Nazarewicz, and D. J. Dean, Eur. Phys. J. A **25**, S01 509 (2005).
[4] G. Stoitcheva, W. Satuła, W. Nazarewicz, D. J. Dean, M. Zalewski, and H. Zduńczuk, Phys. Rev. C **73**, 061304(R) (2006).
[5] A. V. Afanasjev, D. B. Fossan, G. J. Lane, and I. Ragnarsson, Phys. Rep. **322**, 1 (1999).
[6] Yutaka Utsuno, Takaharu Otsuka, Takahiro Mizusaki, and Michio Honma, Phys. Rev. C **60**, 054315 (1999).
[7] I. Y. Lee, Nucl. Phys. **A520**, 641c (1990).
[8] D. G. Sarantites, P.-F. Hua, M. Devlin, L. G. Sobotka, J. Elson, J. T. Hood, D. R. LaFosse, J. E. Sarantites, and M. R. Maier, Nucl. Instrum. Methods Phys. Res. A **381**, 418 (1996).
[9] C. J. Chiara, D. R. LaFosse, D. G. Sarantites, M. Devlin, F. Lerma, and W. Reviol, Nucl. Instrum. Methods Phys. Res. A **523**, 374 (2004).
[10] D. C. Radford, Nucl. Instrum. Methods Phys. Res. A **361**, 297 (1995).
[11] A. Krämer-Flecken, T. Morek, R. M. Lieder, W. Gast, G. Hebbinghaus, H. M. Jäger, and W. Urban, Nucl. Instrum. Methods Phys. Res. A **275**, 333 (1989).

[12] N. R. Roberson and G. Van Middelkoop, Nucl. Phys. **A176**, 577 (1971).
[13] P. B. Vold, D. Cline, M. J. A. deVoigt, Ole Hansen, and O. Nathan, Nucl. Phys. **A321**, 109 (1979).
[14] S. W. Kikstra, C. Van Der Leun, S. Raman, E. T. Jurney, and I. S. Towner, Nucl. Phys. **A496**, 429 (1989).
[15] Balraj Singh and John A. Cameron, Nucl. Data Sheets **92**, 1 (2001).
[16] T. Morikawa, M. Nakamura, T. Sugimitsu, H. Kusakari, M. Oshima, Y. Toh, M. Koizumi, A. Kimura, J. Goto, Y. Hatsukawa, and M. Sugawara, Phys. Rev. C **70**, 054323 (2004).
[17] A. R. Poletti, E. K. Warburton, J. W. Olness, J. J. Kolata, and Ph. Gorodetzky, Phys. Rev. C **13**, 1180 (1976).
[18] H. M. Sheppard, P. A. Butler, R. Daniel, P. J. Nolan, N. R. F. Rammo, and J. F. Sharpey-Schafer, J. Phys. G **6**, 511 (1980).
[19] T. Yamazaki, Nucl. Data Sect. A **3**, 1 (1967).
[20] C. J. Chiara *et al*. (to be published).
[21] J. J. Schwartz, D. Cline, H. E. Gove, R. Sherr, T. S. Bhatia, and R. H. Siemssen, Phys. Rev. Lett. **19**, 1482 (1967).
[22] K. Nakai, B. Skaali, N. J. Sigurd Hansen, B. Herskind, and Z. Sawa, Phys. Rev. Lett. **27**, 155 (1971).
[23] E. K. Warburton, J. J. Kolata, and J. W. Olness, Phys. Rev. C **11**, 700 (1975).
[24] C. D. O'Leary, M. A. Bentley, B. A. Brown, D. E. Appelbe, R. A. Bark, D. M. Cullen, S. Ertürk, A. Maj, and A. C. Merchant, Phys. Rev. C **61**, 064314 (2000).
[25] P. Bednarczyk, J. Styczeń, R. Broda, M. Lach, W. Meczyński, W. Nazarewicz, W. E. Ormand, W. Satuła, D. Bazzacco, F. Brandolini, G. de Angelis, S. Lunardi, L. Müller, N. H. Medina, C. M. Petrache, C. Rossi Alvarez, F. Scarlassara, G. F. Segato, C. Signorini, and F. Soramel, Phys. Lett. **B393**, 285 (1997).
[26] E. Caurier and F. Nowacki, Acta Phys. Pol. B **30**, 705 (1999).
[27] E. K. Warburton, J. A. Becker, and B. A. Brown, Phys. Rev. C **41**, 1147 (1990).
[28] W. A. Richter, M. G. Van Der Merwe, R. E. Julies, and B. A. Brown, Nucl. Phys. **A523**, 325 (1991).
[29] W. Kutschera, B. A. Brown, H. Ikezoe, G. D. Sprouse, Y. Yamazaki, Y. Yoshida, T. Nomura, and H. Ohnuma, Phys. Rev. C **12**, 813 (1975).
[30] Wojciech Satuła, Phys. Scr. T **125**, 82 (2006).
[31] G. Stoitcheva *et al*. (to be published).